PONTIFÍCIA UNIVERSIDADE CATÓLICA
DO RIO DE JANEIRO

Luca Bianco

Startup pipeline flow of thixotropic materials

Dissertação de Mestrado

Dissertation presented to the Programa de Pós–graduação em Engenharia Mecânica of PUC-Rio in partial fulfillment of the requirements for the degree of Mestre em Engenharia Mecânica.

Advisor: Prof. PhD. Paulo Roberto de Souza Mendes

Rio de Janeiro
May 2024

Luca Bianco

Startup pipeline flow of thixotropic materials

Dissertation presented to the Programa de Pós–graduação em Engenharia Mecânica of PUC-Rio in partial fulfillment of the requirements for the degree of Mestre em Engenharia Mecânica. Approved by the Examination Committee:

Prof. PhD. Paulo Roberto de Souza Mendes
Advisor
Departamento de Engenharia Mecânica – PUC-Rio

Prof^a. DSc. Mônica Feijó Naccache
Departamento de Engenharia Mecânica – PUC-Rio

Prof. DSc. Roney Leon Thompson
Departamento de Engenharia Mecânica – UFRJ

Rio de Janeiro, May 8th, 2024

Luca Bianco

Luca Bianco graduated in Mechanical Engineering in 2020. Now, he's pursuing a Doctorate in Mechanical Engineering at PUC-Rio and a Professional Specialization in Artificial Intelligence and Machine Learning at PUC-Minas.

To my beloved parents.

Acknowledgments

First and foremost, I would like to express my deepest gratitude to God, Jesus Christ, and my faith for providing me with everything I needed to complete this stage of my life.

To Prof. Paulo, my advisor, for his unwavering support, guidance, encouragement during the course of this work and for opening the doors of his laboratory to me and giving me the opportunity to learn about rheology.

To my parents, Andrea and Alfonso, and my family, towards whom I am profoundly grateful and indebted. Without their help and constant support, I wouldn't have achieved anything in my life.

To my childhood friends in Italy. Despite the distance and the time that has passed, I miss all of you.

To Leonardo Zurita, for helping me in challenging moments with his expertise in operating lathes.

To Elias da Conceição Rodrigues, Behbood Abedi, Pouya Khalili, and Isabela Soares, for the great time that we spent together talking about life and rheology at GREO.

To all friends from the Laboratory of Micro Hydrodynamics and Flow in Porous Media (LMMP) at PUC-Rio.

To Profa. Mônica Naccache, Priscilla, Eduardo Leiva-Mateus, Henrique, José, Gabriel, Eliana, Lorena, Matheus, Vanessa, Yago, Lara, Igor, Gabriel Elias, Marina, Gabriela, Pedro, Patricia, Rodrigo, Alexandre, and Monica for all the productive conversations and good moments that we had at the Group of Rheology (GREO).

To Prof. Florian Pradelle and Carina Beline from the Department of Mechanical Engineering at PUC-Rio for their constant support and help.

To all the professors from the Department of Mechanical Engineering at PUC-Rio.

To Cida and Leandro, from the Padre Laércio Building at PUC-Rio.

To Eraldo and all the bus drivers of 1001 who operate the route from Charitas to Gávea every day.

To all the kind people I've encountered in my life over these two years. Although I can't remember everyone's name, I'm deeply grateful for helping me so much during this journey.

Abstract

Bianco, Luca; Mendes, Paulo Roberto de Souza (Advisor). **Startup pipeline flow of thixotropic materials**. Rio de Janeiro, 2024. 65p. Dissertação de Mestrado – Departamento de Engenharia Mecânica, Pontifícia Universidade Católica do Rio de Janeiro.

Understanding the mechanical response of time-/strain history-dependent materials is essential for various industrial applications, notably in pipeline transportation. These materials exhibit complex rheological behavior, that hugely influence their flow characteristics. Despite decades of research, accurately modeling the mechanical behavior of these materials remains a challenge, with existing models often constrained by their inability to predict complex responses beyond simple shear flow configurations. Consequently, there is a pressing need for further investigation to refine our understanding and predictive capabilities in this field, ensuring the efficient and safe operation of industrial processes involving such materials. This work aims to investigate the flow restart of thixotropic fluids through both numerical and experimental methods. Specifically, this study involves modeling a thixotropic Laponite suspension 1.25% wt using a constitutive equation that faithfully accounts the real material's behavior during processes that induce microstructural breakage or construction. Numerical simulations were used to analyze the restart processes in a pipe using the modelled suspension and compare it with a suspension present in the literature modelled with the same mathematical model to understand the role of thixotropy in the flow restart. Additionally, an attempt to validate the constitutive equation obtained was made. The numerical analysis indicated that both fluids exhibited similar qualitative behavior for the temporal fluidity evolution. While high thixotropy caused a gradual transition from rest to flow, low thixotropy resulted in sudden transitions. Higher imposed pressure gradients were associated with earlier resumption of flow and larger sheared regions across the spatial domain for both fluids. Additionally, for both fluids, the steady-state regime was solely defined by the imposed pressure gradient. Despite the limitations of the experimental apparatus and the notable differences between the numerical predictions and experimental results for the Laponite suspension formulated in this work, the mathematical model employed showed to be a useful tool to study the restart flow of thixotropic fluids.

Keywords

Thixotropy; Flow restart; Viscoplasticity.

Resumo

Bianco, Luca; Mendes, Paulo Roberto de Souza. **Recomeço de escoamento em duto de materiais tixotrópicos**. Rio de Janeiro, 2024. 65p. Dissertação de Mestrado – Departamento de Engenharia Mecânica, Pontifícia Universidade Católica do Rio de Janeiro.

Compreender a resposta mecânica de materiais dependentes do tempo / histórico de deformação é essencial para várias aplicações industriais, especialmente no transporte por dutos. Esses materiais exibem um comportamento reológico complexo, que influencia enormemente suas características de escoamento. Apesar de décadas de pesquisa, os modelos existentes muitas vezes são incapazes de prever com precisão respostas complexas além do escoamento simples de cisalhamento. Consequentemente, há uma necessidade urgente de investigação para refinar a compreensão e a capacidade preditiva nesse campo, a fim de garantir operações eficientes e seguras de processos industriais envolvendo o escoamento desses materiais. Este trabalho tem como objetivo investigar o recomeço de escoamento de fluidos tixotrópicos por meio de métodos numéricos e experimentais. Especificamente, este estudo envolve a modelagem de uma suspensão de Laponite tixotrópica 1,25% wt usando uma equação constitutiva que representa fielmente o comportamento real do material durante processos que induzem quebra ou reconstrução microestrutural. As simulações numéricas foram utilizadas para analisar processos de reinício de escoamento em dutos usando a suspensão modelada neste trabalho, comparando-a com uma suspensão presente na literatura modelada com o mesmo modelo, objetivando compreender o papel da tixotropia no reinício do escoamento. Além disso, foi realizada uma tentativa de validar a equação constitutiva obtida. A análise numérica indicou que ambos os fluidos exibiram comportamento qualitativo semelhante para a evolução temporal da fluidez; enquanto uma alta tixotropia causou uma transição gradual do repouso para o escoamento, baixa tixotropia resultou em transições súbitas. Altos gradientes de pressão impostos foram associados a menores tempos de reinício e regiões cisalhadas maiores ao longo do domínio espacial para ambos os fluidos. Adicionalmente, para ambos os fluidos, o regime permanente do escoamento foi unicamente definido pelo gradiente de pressão imposto. Apesar das limitações do aparato experimental e das notáveis diferenças entre as previsões numéricas e os resultados experimentais para a suspensão de Laponita formulada neste trabalho,

o modelo matemático empregado mostrou-se uma ferramenta útil para estudar o reinício de escoamento de fluidos tixotrópicos.

Palavras-chave

Tixotropia; Recomeço de escoamento; Viscoplasticidade.

Table of contents

List of figures

List of tables

"We've got to get in to get out"

Genesis, *The Carpet Crawlers*.

1
Introduction

In this introductory chapter it will be presented the object of study of this work. Its motivation is contained in sections 1.1, 1.2 and 1.3, where the classification and relevance of the typology of the fluids studied in this dissertation are presented in conjunction with the restart flow problem. Furthermore, the literature review is presented in section 1.4. Finally, the research goals and the dissertation organization is presented in section 1.5.

1.1
Categorization of fluids behavior

The analysis of rheological parameters of complex soft glassy materials represents a primordial step of any scientific investigation ment to asses its flow behavior. In the context of rheology, materials can be evaluated by means of physical properties that arise by analyzing the existing relationship between the applied stress and the resulting fluid kinematics in simple shear or elongational flows, known as material functions. Two categories of materials can be defined by subdividing materials with material functions dependent (or independent) on time and dependent (or independent) on the structural rearrangement caused by previously experienced deformations (i. e. its strain history), as showed in Tab. 1.1.

Time-/strain history-independent	Time-/strain history-dependent
Newtonian	Irreversible
Shear thinning	Thixotropic
Shear thickening	Antithixotropic
Viscoplastic	Viscoelastic

Table 1.1: Fluid taxonomy

Materials that do not show dependence on time and strain history posses a single physical parameter to be determined: the viscosity, being it dependent on the shear rate or not, defined by $\eta(\dot{\gamma}) = \tau(\dot{\gamma})/\dot{\gamma}$; Newtonian fluids possess constant viscosity, regardless of the applied shear stress; shear thinning fluids display a viscosity decrease for increasing values of applied shear stress; shear thickening fluids experience a viscosity increase with increasing values of shear stress. Viscoplastic materials are the only exception for this statement, where an additional parameter is of significant interest: the minimum shear stress for which the material starts to flow, popularly known as yield stress, τ_y.

On the other hand, time-/strain history-dependent materials exhibit a more complex rheological response that cannot be represented solely by the material's

viscosity, and can be further subdivided in four other physical responses, namely, thixotropy, antithixotropy, viscoelasticity and irreversibility. Thixotropy is characterized by a reduction in the material's apparent viscosity when subjected to a shear stress sufficiently high to be able to promote a breakdown of its microstructure, followed by viscosity restoration upon the cessation of shear, attributed to the spontaneous reformation of the material's microstructure [3]; antithixotropy is the exact opposite of thixotropy, characterized by a reversible viscosity increase with application of a shear stress; whereas, irreversibility configures a rheological response that includes an irrecoverable variation of the material's physical properties due to a permanent microstructural rearrangement imposed by a given strain history that the material undergone; viscoelasticity is characterized by a time and strain dependent rheological behavior, resembling both viscous fluids and elastic materials, caused by the competition of energy dissipation due to viscous friction and storage of elastic potential energy promoted by macromolecular structures that integrate the material [4, 5]. Although the presented subdivision is useful in the context of rheological characterization, complex materials in nature and industry may exhibit a rheological behavior that does not fit exactly into a single category, potentially exhibiting a subset of these rheological responses.

Despite the relevance of time-/strain history-independent fluids, materials that exhibit time and shear history dependence posses a crucial role in great part of contemporary economical activities. Its relevance is evidenced by its ubiquitousness in today's industrial landscape, with applications ranging from the food to the energy industry [3]. In this context, a case of special interest is the pipeline transportation of such materials, once it displays a continuum, economical and environmentally sound form of transportation.

1.2
Pipeline transportation of time-/shear history-dependent materials in contemporary industrial activities

The transportation of time-/strain history-dependent materials by means of pipelines represent the main option to transport it in large scales. The rheological properties of these fluids possess great impact in the process, due to its fundamental role in determining the flow kinematics. Several examples of this relevance can be encountered in the literature; some of them can be used as representative examples, as will be showcased below.

Knowing that 20% of the global oil reserve is comprised by waxy crudes [6], deep and ultradeep offshore exploration of crude oils represent a great font of revenue for the global oil and gas industry. In fact, a recent survey on the global oil and gas exploration published in 2021 [7] pointed that large and medium-sized fields

with 85% of recoverable reserves were mainly discovered in deep and ultradeep offshore environments. When a planned or unplanned shutdown of a deepwater offshore pipeline transporting waxy crude oil occurs, the oil is forced to cool to the temperature of the seabed; generally, a temperature below the Wax Appearance Temperature (WAT). Such event will lead the crude to gelify, due to the growth and interlock of wax crystals, conferring the material a time-dependent yield stress behavior. Consequently, the analysis of the relation between the time dependent feature of the material and the process macroscopic variables in the pipeline turns to be of paramount importance for planning successful operational procedures, once the rheological characteristics of the fluid are known to be one of the major factors ruling its response to pressure gradients [8].

Known as the industrial activity with the largest production of waste, the mining industry relies major concerns in strategies related to the disposal of its operational residues [9], due to the high toxicity of its compounds and its prolonged harmful impact to the environment [10, 11, 12]. In fact, disasters linked to mining residue's dam failures have proved to provoke irretrievable losses, including the loss of human lives and assets, and severe damages to endemic fauna and flora [13]. A possible alternative to reduce the occurence of such ambiental disasters is to retrieve water from the mine tailing slurries and dispose it in its novel paste-like form, which not just will prevent it from flowing easily but also provide a great source of economical savings related to the recycling of water and recover of waste and caustic materials [9]. Nonetheless, pastes of mine tailings possess non-Newtonian time-dependent behavior that needs to be taken into account in the design phase of pipe facilities, in order to guarantee operational efficiency and safety [14, 15].

It is estimated that approximately $330\,\mathrm{km}^3$ of wastewater are annually produced worldwide and, due to the presence of water, organic matter and nutrients in its composition, wastewater sludges are considered potential economic assets [16]. Despite populational growth is expected to reduce its pace by the end of the 21th century, the global population is expected to grow, concurrently with good's consumption [17, 18]; thus, the production of waste is also expected to rise. Due to its complex composition conferred by the formation of amorphous filamentous structures of bacterial origin [19], dewatered sewage sludges exhibit thixotropic behavior [20] and the assesment of its rheological properties are vital to the design of its pumping and transportation facilities [21].

Remarkably, cement is deemed as one of the most important construction materials of the world [22]. Its main application is the production of concrete, that can account to 60% of the total of materials used in the construction of a building [23]. Whether to execute the construction of megatall buildings such as the Burj Khalifa [24], wellbore cementing [25] or to accomplish the 3D printing of ordinary

buildings [26, 27], the time-dependent rheological characteristics of fresh cement pastes play a central role in concrete flow, which directly impacts processes efficiency [28].

As could be read in the above paragraphs, the fluid's complex rheology has a direct impact in the processes efficiency and security, and it is an essential information to be taken into account during the design of pipeline facilities and the planning of its correlated operations. In particular, when the material response includes viscoplasticity in addition to other time-/strain history-dependent behavior, a challenging scenario of high industrial interest is reported in the literature: the pressure-driven flow restart of these fluids in pipelines.

1.3
The flow restart of time-/strain history-dependent materials in pipelines

The pressure-driven restart flow procedure of time-/strain history-dependent yield stress materials has been imposing great challenges among industrial applications that involves its pipeline transportation, that may result in overestimations or irreparable losses [29, 30, 31].

Briefly, it comprises to impose a sufficiently high pressure gradient able to yield the structured fluid, in order to reset the flow and, subsequently, attain the steady-state regime relative to the process condition prior to the flow shut-in, within a reasonable amount of time.

A set of research lines have been dedicated to unveil the existent relationship between the rheological features of soft glassy materials and its process macroscopic variables. Within the context at hand, the analysis of the yielding behavior in simple shear flow, the analysis of the restart procedures promoted by an imposed pressure difference in pipelines and the mathematical modelling of the rheological characteristics of these materials can be deemed as topics of central importance.

1.4
Literature review

In order to assess the current knowledge concerning the pressure-driven restart flow of complex fluids that possess both time and shear-history dependency, it is proposed to subdivide the literature review in two separate parts, in accordance with the conclusions made in sec. 1.3:

1. analysis of the yielding and flow behavior in simple shear and pressure-driven flow conditions (sec. 1.4.1);

2. mathematical modelling of the involved physical phenomenons (sec. 1.4.2).

1.4.1
Yielding and flow behavior of time-/shear history-depenent materials in simple and Pressure-driven restart flows

The analysis of the yielding behavior in simple shear flow at different time and lengthscales and in pipelines, both numerically and experimentally, have been deemed a valuable tool to detect typical characteristics of the yielding transition of complex fluids.

Analysis of creep tests has been performed in order to elucidate the relationship between the macroscopic response and particle dynamics of soft glassy materials. Numerical analysis advocated that exist a proportional relationship between particles' motion and the macroscopic strain, where the yielding transition was characterized by the appearance of heterogeneously distributed spots of enhanced particles' mobility promoted by the large displacement of few particles in the domain, where the onset of flow corresponded to the manifestation of a spot with enhanced local movement [32], that may be related to localized plastic rearrangements occurring prior to the onset of fluidization, of the order of magnitude of the material's structure, that will eventually lead the material to undergo a yielding transition [33]. Also, the pre-yield phase of a delayed flow restart has been reported to be marked by an initial solid elastic deformation, followed by creep, in which Brownian motion played a key role, being responsible to assist the microstructure's bond rupturing, enabling the material to creep and, eventually flow, provided that the imposed stress was greater than a threshold stress value [34], corroborating with experimental observations reported by [35] and [36].

The material's yielding transition is tightly related to its time-dependent structural evolution [37], where long rheological transient regimes are linked to flow conditions with hydrodynamic and colloidal bond's attractive forces of comparable magnitude [36]. In fact, it has been noticed that thixotropic effects turn to be more relevant when the time of a shear rate step was within an order of magnitude in comparison to the material's diffusive time of a single particle; that is, when Brownian motion starts to be relevant [35]. Also, the imposed stress was in charge of dictate the restart attempt fate, that could lead to one of three possible scenarios: a succesful restart with negligible creep before yielding, a succsesful restart with appretiable creep before yielding or an unsucsessful restart. In turn, the characteristic times of flow inertia and microstructural change were in charge to determine the qualitative behavior of both the creep and yielding phase [38]. The macroscopic delayed yielding phenomenon have been reported to consist in a 3-step process [35, 36]: first, the material undergoes creep and, subsequently, the material gets progressively fluidized by the action of stress and attains full fluidization. The instants of conclusion of each step have been considered characteristic times of the process

[35]; a timescale representing the creep duration, and a timescale representing the time to the material attain full fluidization.

Multiple yield stress values have been encountered for time-dependent materials, each linked to a corresponding material's structural state [3, 39]: the critical value that will promote a microstructural breakage sufficiently large to enable the material to be fluidized, originally in its fully structured state, is known as static yield stress; the minimum value of shear stress capable to sustain flow has been coined as dynamic yield stress. Chang and Boger [40] defined two distinct critical stress values linked to the restart process of waxy crude oils: the elastic-limit yield stress, defined as the maximum stress value for which only elastic deformations could be expected, and the static yield stress, the stress value that must be overcame in order to promote both plastic deformations and the material's fracture; for stress values laying between elastic-limit and static yield stress, the material experience viscoelastic creep; so, the authors came to the conclusion that the yielding process of waxy crude oils in a stress ramp regime is composed by a sequence of three events: elastic deformation, viscoelastic creep and breakage. Interestingly, by analysing stress ramp tests data of gelled waxy crudes, Fakroun and Benkreira [41] concluded that a stress value higher than the static yield stress denominated fragmentation stress, demarking the end of the gel microstructural fracture process and start of viscous flow, rather than the static yield stress, was a more accurate predictor of flow onset.

Cunha, de Souza Mendes and Siqueira [1] numerically investigated the influence of the initial microstructural state of the material and the plastic number, *Pl* (i. e. the ratio between the yield stress and the maximum stress in the physical domain [42]) in the pressure-driven pipe flow of a thixotropic viscoplastic material, mathematically described by the fluidity constitutive model proposed by de Souza Mendes, Abedi and Thompson [2]. The authors noticed that the material's plasticity, represented by *Pl*, prescribed both the fluid's velocity and structural level fields at steady-state, being the steady-state regime uniquely defined by the applied stress and independent of the initial structural condition of the material. Similar experimental findings were registered by Wang et al. [43] that studied both the steady-state flow and transient restart of waxy crude oil models in an experimental pipeline apparatus. By analyzing the data presented by the authors, it could be estimated that for the case of isothermal restart procedures with different initial microstructural states, the steady-state flow regime was uniquely defined by the imposed stress (i.e. in the context of this article, the imposed flow rate).

Comparisons between restart procedures in pipelines involving purely viscoplastic and thixotropic fluids have been used to assess the influence of the microstructural evolution in the process. By comparing the velocity profiles over time

of two materials by Ultrasonic Doppler Velocimetry (UDV), Moisés et Al. [44] noticed that the purely thixotropic material (a laponite suspension) exhibited a delayed restart, as also a delayed achievement of the steady state regime, in comparison to the purely viscoplastic one (a carbopol solution). Abedi et Al. [45] reached similar conclusions, where the predictions of flow rate furnished by a Herschel-Bulkley fit of steady-state data of a purely viscoplastic material (a commercial hairgel) showed an almost perfect match with experimental measurements made in an experimental apparatus composed by a pipe with grooved walls, whilst the numerical and experimental computations for a purely thixotropic fluid (a laponite suspension) showed great divergence; the authors concluded that its thixotropic feature was the cause of such discrepancy, by preventing the flow's development within the time and lenghtscale of the experimental observations.

During this brief review, critical stress and strain values, as also characteristic times, have been reported as physical quantities that demark the departure from an elastic solid-state to a fluidized one, as a consequence of the transient variation of the material's microstructural state. Moreover, it was noticed that the material's yielding configures a complex process that characterizes its time-dependent response. In face of these evidences, it can be stated that, in the context of flow restart, in addition to the minimum load to be applied to fluidize a fully-structured material, another basic information is needed to fully characterize the yielding process: how the microstructural breakage succeeds till the achievement of the steady-state regime. Thus, it is natural to affirm that mathematical models formulated in the aim of represent the behavior of time-/shear history-dependent materials have to include this information in its formulation, in order of expect to faithfully describe the real behavior of the material.

1.4.2
Phenomenological mathematical modelling of complex soft glassy materials

Mathematical models capable of faithfully represent the response of real complex fluids reported in the works analysed in sec. 1.4.1 are an old desire of the international rheology community. In fact, since the firsts observations of the thixotropy phenomenon made by Schalek and Szegvary [46] on metal oxide gels that date back to decades contemporary to the coining of the term "rheology", several attempts have been made. It has received significant attention in the last decades [47] where, among the available physical frameworks used to model this physical response, structural kinetics models [48] emerged as a practical option in modeling such behavior, once its formulation includes solely a mathematical description of the material's physical behavior pertaining the macroscale, whose information about

its microstructural state are generally condensed into a single parameter responsible to represent its structuring level [49]. Generally, such models posses a constitutive equation whose material functions are defined to be dependent on the structuring level, that posses its respective evolution equation. Generally, constitutive equations for TEVP materials often posses a high level of complexity that is translated in the presence of a great number of parameters [50] often lacking a clear physical foundation, that will need to be determined from an extensive set of experiments and fitting procedures; in industrial applications, specially in the oil and gas field, such fact is reflected in the tendency in utilize simpler models with lower prediction capability, due to its relative lower complexity [51].

The first work dates back to Goodeve and Whitfield [52], where an attempt was made to propose a quantitative measure of thixotropy. The authors proposed that the temporal rate of increase of the structuring level of a thixotropic material could be defined as $\frac{dx}{dt} = k''(x_m - x)^a$, where x is the material's structuring level, x_m the maximum achievable value of x and a the order of this process. Also, the rate of decrease of the structuring level was defined as $\frac{dx}{dt} = -ksx$, where k is a positive constant and s the shear. A connection between the microstructural state and the apparent viscosity value was proposed by the authors, suggesting that the apparent viscosity η of the material could be expressed as the summation between a residual viscosity η_0 and the product of a positive constant k' with the same units of viscosity and the structural level (eq. (1-1)).

$$\eta = \eta_0 + k'x \tag{1-1}$$

In a subsequent publication, Goodeve [53] deduced an evolution equation for the concentration of links n promoted by shear (i.e. the chosen structural parameter) as sum of link's concentration rate between the link's formation and breakage rates (eq. (1-2)),

$$\frac{dn}{dt} = \underbrace{k''(2n_0 - 2n)^2\sigma}_{\text{Link formation}} \overbrace{-\frac{nHz\sigma}{f_c}}^{\text{Link breakage}}. \tag{1-2}$$

In this work, Goodeve stated that, considering that the material could be divided in layers of thickness z composed by particles forming the microstructure of the structured material, and that the extension of the distance between the particles' layers moving in simple shear was given by the well known Hooke's law, the rate of link breakage by shear could be defined as the ratio between the concentration of links, n, per unit link's lifetime, $t_c = f_c/Hz\sigma$, where n_0 is the number of links per particle, σ the rate of shear, H the spring constant and f_c the minimum force to promote the breakage of a link. The term related to the formation of links was derived from previous works on the enhancing of coagulation rate during shearing,

where $(2n_0 - 2n)$ represents the potential partners to a link[1]. As will be see in the next two paragraphs, despite its simplicity, similar ideas utilized in these two seminal works were utilized in more recent publications.

Acierno et Al. [54] formulated a non-linear model based on the Maxwell viscoelastic model with relaxation times and stress relaxation moduli dependent on the material's structuring level (eq.(1-3 - 1-5)),

$$\frac{1}{G}\tau + \lambda\frac{d}{dt}\left(\frac{1}{G}\tau\right) = 2\lambda D, \tag{1-3}$$

$$G = G_0 x \text{ and } \lambda = \lambda_0 x^{1.4}, \tag{1-4}$$

$$\frac{dx}{dt} = \overbrace{\frac{1}{\lambda}(1-x)}^{\text{Link formation}} \underbrace{-ax\frac{1}{\lambda}\sqrt{\frac{E}{G}}}_{\text{Link breakage}}, \tag{1-5}$$

where λ is a relaxation time pertaining to the relaxation spectrum, τ the stress tensor, D the rate of strain tensor, x the structural parameter, G_0 and λ_0 the G's and λ's values at the linear viscoelastic limit, E the elastic energy defined as $E = \frac{1}{2}tr(\tau)$, where $tr(\tau)$ is the trace of the stress tensor, and a a constant parameter. For the evolution equation of the structural parameter (eq. (1-5)), x, as in the previously cited publications, the time-dependent structural evolution was defined as the sum of the processes of structural formation and breakage. While the breakage term was formulated considering how a single molecule composing the system interact with the surrounding others in steady shear flow, the term related to the formation of links was formulated using idealized assumptions.

Mujumdar et Al. [55] proposed the TEVP model shown in eq.(1-6 - 1-8):

$$\tau = \tau_e + \tau_v \tag{1-6}$$

$$\frac{d\lambda}{dt} = \underbrace{-K_1\dot{\gamma}_+\lambda}_{\text{Breakage term}} + \overbrace{K_2(1-\lambda)}^{\text{Construction term}} \tag{1-7}$$

$$\gamma = \begin{cases} \frac{\partial\gamma_e}{\partial t} = \dot{\gamma}, & |\gamma_e| < \gamma_c(\lambda) \\ |\gamma_e| = \gamma_c(\lambda), & |\gamma_e| \geq \gamma_c(\lambda) \end{cases}. \tag{1-8}$$

$$\dot{\gamma}_+ = \begin{cases} 0, & \dot{\gamma}\gamma_e \leq 0; \\ |\dot{\gamma}|, & \dot{\gamma}\gamma_e > 0; \end{cases}. \tag{1-9}$$

where $\tau_e = \lambda G\gamma_e$ is the material's elastic contribution to the total stress and $\tau_v = (1-\lambda)K\dot{\gamma}^n$ its viscous counterpart. K, K_1 and K_2 are positive constant parameters, $\dot{\gamma}_+$ is the shear rate's magnitude in the post-yield phase, defined by

---

[1]The reader is invited to consult the original source for more details.

eq. (1-9), γ_e is the elastic strain, λ is the structural parameter, G the elastic modulus, $\gamma_c = \gamma_{co}\lambda^m$ the critical strain to onset the microstructural breakage, γ_{co} the material's critical strain related to the undisturbed state prior to the application of any load and m a constant parameter related to the material. In this paper, the parameter λ was utilized to specify the structural level of the material, that could assume a value of 1 to represent a totally structured material, and 0 to denote a totally unstructured one. For the evolution equation of λ (eq. (1-8)), the destruction process was considered to be a simple function of the shear rates' magnitude and the material structural level. Furthermore, the construction process was assumed to be dependent only on the actual structural level.

Mewis and Wagner [48] reviewed the evolution of the mathematical modelling of thixotropy and perceived that a great amount of inelastic kinetic models could be molded into a general framework inspired on its real physical features. Remarkably, they concluded that the majority of the proposed constitutive equations assumed that exist a linear relationship between the materials rheological parameters and its structural state. That is, simplistic functions have been chosen to describe the breakdown and buildup processes of thixotropic materials. The microstructure's state have been mostly modeled according to its qualitative response to an applied load, where the mathematical formulation of the time evolution of the microstructure's state of a structured material under flow have been usually formulated under the criteria of "simplicity" [56].

de Souza Mendes and Thompson [57] classified the existing models in two categories, namely, Type I and Type II. According to the authors, type I models originates from the Bingham model and are composed by an algebraic viscoplastic stress equation whose elastic behavior is introduced by defining that the material will behave like a hookean solid to stress values below the yield stress, and posses material properties expressed as functions of a structure paramenter λ, that specifies the microscopic state of the material. In turn, Type II models are based on classical viscoelastic models and posses a differential stress equation whose material properties are defined to be functions of λ. They concluded that type II models can be considered general models that can be simplified in order to model special cases of the thixotropic elastoviscoplastic (TEVP) response to an applied stress, and are in agreement with the concept of considering that the yield stress is a quantity related to a material in its fully structured state and every mechanical component pertaining to the mechanical analog of the model have a clear physical nature. Furthermore, it was noted that constitutive models for time and shear history dependent fluids can be grouped by the chosen agent of microstructural breakdown [47]; that is, wheter the structure parameter is a function of the strain rate, $\dot{\gamma}$, or the stress, σ. de Souza Mendes and Thompson [57] argued that considering the stress value as

the microstructural breaking agent is a more physically consistent choice, once a minimum force higher than the interparticle force that enables the system to stay interconnected must be applied to promote its breakage.

De Souza Mendes [56] proposed a TEVP model inspired in the linear viscoelastic Maxwell constitutive equation with both viscous and elastic contributions set to be dependent on a structural parameter λ that could assume values between 0 (totally unstructured state) and 1 (totally structured state). The author used physically consistent arguments to define the characteristics that the involved material functions had to possess in order to return predictions faithful to the real rheological response. A remarkable characteristic of the model is contained in the fact that the evolution equation for λ is formulated to yield to time-independent structural state's in accordance to the steady-state regime specified by the material's flow curve; the rationale behind this choice is to utilize the flow curve to obtain the equilibrium structural state relative to the given applied load magnitude, assuming that the flow curve specifies the stable equilibrium states of the mechanical analog [58]. Also, the shear stress, rather the shear rate, is considered the microstructural breakdown agent, in contrast to the great majority of the available TEVP models to date. Another TEVP model was proposed in de Souza Mendes [59] following the same physical assumptions previously made in [56]. But, this time, a Jeffrey-like mechanical analog was used to define the stress equation, which allowed the inclusion of a structure-dependent retardation time without yielding to a growth of the set of parameters of the model; both models proposed in [56] and [59] were capable of represent apparent yield-stress materials only. Posteriorly, de Souza Mendes and Thompson [60] gave sequence to the work done in [56] and [59] by formulating the related material functions such that to enable it to be capable of model true yield stress materials, where the zero-shear rate viscosity is expected to possess an infinite value.

Remarkably, in [2] it was proposed a novel TEVP phenomenological constitutive model of type II where the state of the material's microstructure is defined by the fluidity (i.e. the reciprocal of viscosity) that obeys an evolution equation whose terms can be obtained through standard rheological experiments instead of the usual structure parameter. Such approach in modelling the thixotropic behavior of the material depart considerably from the constitutive equations available in the literature for TEVP materials, once it does not include any auxiliary variable to describe the microstructural state and proved to successfully reproduce complex phenomenons relative to a TEVP response, such as the avalanche effect and transient shear banding [1].

As could be read in the above paragraphs, even though its mathematical modelling have been an active research line for decades, the response of these materials have been modeled according to its qualitative behavior in its great majority, demon-

strating that, despite the great effort dedicated to formulate consistent constitutive equations, their mathematical modeling is still an open problem [3]. Additionally, the existing models have not been tested for flow configuration other than simple shear flow, with rare exceptions.

1.5
Research goals and organization of the dissertation

The main goal of this work is to investigate the flow restart of thixotropic fluids by numerical and experimental means. To achieve it, three specific subgoals are delineated below:

1. To model a thixotropic Laponite suspension 1.25 % wt, that will be presented in sec. 3.1, with the constitutive equation proposed by de Souza Mendes et Al. [2], due to its fidelity to the real processes of microstructural breakdown and reconstruction of the material;

2. To numerically simulate and analyze restart processes in a pipe of the Laponite suspension presented in the first subgoal, promoted by a constant pressure gradient applied at its inlet, and compare the material's qualitative behavior with the qualitative behavior of a Laponite suspension studied in [2], in order to understand the role played by thixotropy in the flow restart;

3. To validate the mathematical model in an experimental apparatus, aiming to evaluate its predictive capability.

This work will be organized into the following chapters: Chapter 2 will encompass all experimental activities; Chapter 3 will detail the mathematical formulations employed to model the rheological behavior of the fluids and the flow restart; Chapter 4 will define the numerical procedures utilized to solve the mathematical problems presented in Chapter 3; Chapter 5 will present the results and related discussions; finally, Chapter 6 will resume the conclusions obtained in this dissertation and propose future works.

2
Experimental procedures

In this chapter, a description of the experimental procedures performed in this work are described. First, an explanation of the fluid preparation and rheometrical experiments are presented. In sequence, a description of the flow experiments in a experimental apparatus is given.

2.1
Fluid preparation

The fluid that will be utilized in the experimental apparatus is a Laponite suspension 1.25 % wt that was prepared following a similar protocol utilized by Abedi [61]: in a container with 3830 ml of deionized water under constant mixing by an overhead stirrer equipped with a 3-blade impeller at 300 rpm, 110 ml of a 0.04 mol/l deionized water solution of NaOH was added. In sequence, 50 g of previously filtered and baked (at 120°C for 4 hours) Laponite powder was added to the container and the stirrer was set to 450 rpm for 30 minutes. Finally, 10 ml of a 0.4 mol/l deionized water solution of NaCl was added to the container and the mixing process is let for more 30 minutes. At the end of this time period, the stirrer is turned off, the container is closed and let to rest sheltered from direct light sources for a sufficient amount of time to gellify at room temperature. The final product is a transparent gel that posses an appreciable yield stress and exhibit thixotropic features; a sample of the prepared fluid is shown in Fig. 2.1.
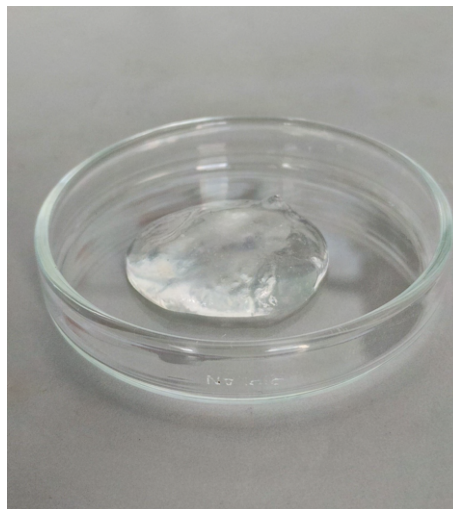
Figure 2.1: A small sample of the Laponite suspension 1.25 % wt prepared for the experiments in the experimental apparatus

2.2
Rheometrical devices and experiments

A concentric cylinders geometry with grooved walls was used to perform the rheometrical tests (Fig. 2.3a and 2.3b), with exception to steady state flow curve tests for $\dot{\gamma} > 900$, where a DIN concentric cylinders geometry with smooth surfaces was used (Fig. 2.2a and 2.2b); all tests were performed at 22 °C. All tests using the grooved geometry were performed in a AR-G2 rheometer from TA instruments; the tests with the smooth geometry were performed in a DHR-3 rheometer from TA instruments. Before the beginning of each test, a sample loading protocol was strictly followed, aiming to ensure that the same initial structuring level of the sample was achieved, in order to guarantee repeatability, as described next.

The geometry is raised to the loading position (100000 μm) and a reasonable amount of sample is placed inside the geometry (approximately 23 ml) and 1 minute is waited. Then, the gap is set to 9000 μm and 8 minutes are waited. Finally, for both of the geometries, the gap is set to the test gap (4000 μm for the grooved and 5912.87 μm for the DIN geometry with smooth walls). Finally, a simple cover is placed and the experiment is started.

Each test in the rheometer consists of two parts. In the first part, right after the test starts, an additional time of 900 s is waited to guarantee that the sample temperature is equal to the set temperature specified in the test description in the rheometer's software. Then, a constant shear rate of $700 \ s^{-1}$ is imposed and is set to last till the achievement of a steady-state regime; this stage was included in the test's plan in order to erase the strain history imposed to the sample during its loading process in the rheometer's cup.

Right after this pre-shear phase, a certain amount of time must be chosen to let the sample rest, enabling its microstructure to rebuild. In order to obtain this time period it was performed a time sweep test, presented in Fig. 2.4, with oscillatory frequency of 1 Hz and strain amplitude of 1%. From this test, it was concluded that a period of 3600 s was sufficient to let the microstructure reconstruct albeit the G^* data indicates that the microstructure's build-up process persists even after 40000 s; ideally, it shoud be waited a time period that must coincide to the total reconstruction of the sample's microstructure (i. e. when G^* assumes a constant value). Nonetheless, as will be noticed in all rheometrical results, not just the chosen time period, but the whole pre-test protocol, was able to provide tests with excellent repeatability, demonstrating that the chosen rest time and pre-test protocol enables to attain the same microstructural state at the beginning of each test.

(a) Smooth bob mounted in the DHR-3 Rheometer
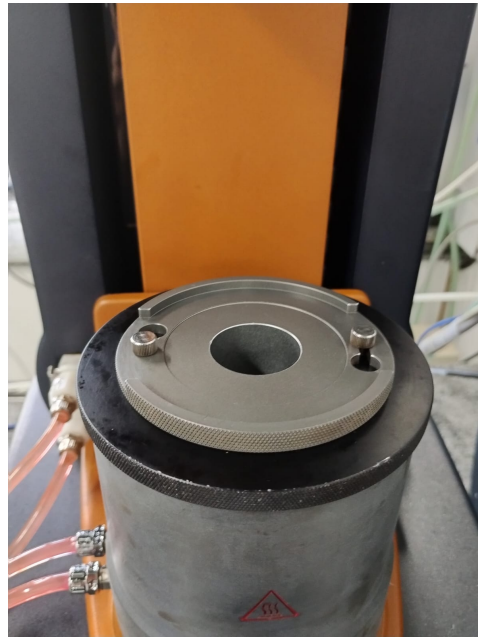
(b) Smooth cup mounted in the DHR-3 Rheometer

Figure 2.2
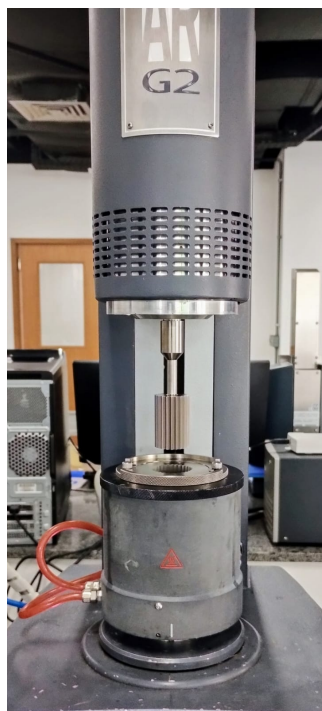
(a) Grooved bob mounted in the AR-G2 Rheometer
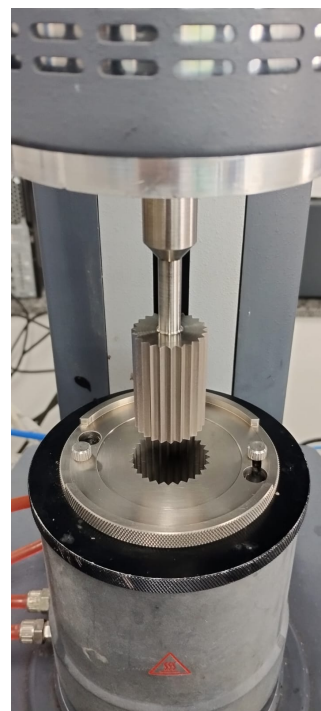
(b) Grooved bob and cup mounted in the AR-G2 Rheometer

Figure 2.3

Since the value of oscillatory strain amplitude was not based on any physical argument, it must be checked whether the strain amplitude value of 1% disturbs the sample's microstructure during the time sweep test from the beginning of the test. To achieve this goal, an amplitude sweep test was performed, imposing an oscillatory shear amplitude range both below and above 1%. The output of this test is also shown in Fig. 2.4, where it can be seen that for values of amplitude strain lower than 1.58 % the resultant complex modulus is nearly equal to the previously performed time sweep test output, showing that for this range of amplitude strains, the microstructures stays undisturbed and only the process of construction of the microstructure occurs. For amplitude strain values higher than 1.58 %, a decrease in the value of G^* is noticed, indicating that the sample is experiencing a microstructural breakage process. These results confirms that the value of 1% of amplitude shear strain does not disturb the sample's microstructure and the time sweep test showed in Fig. 2.4 is capturing solely the material's microstructural rebuild process.
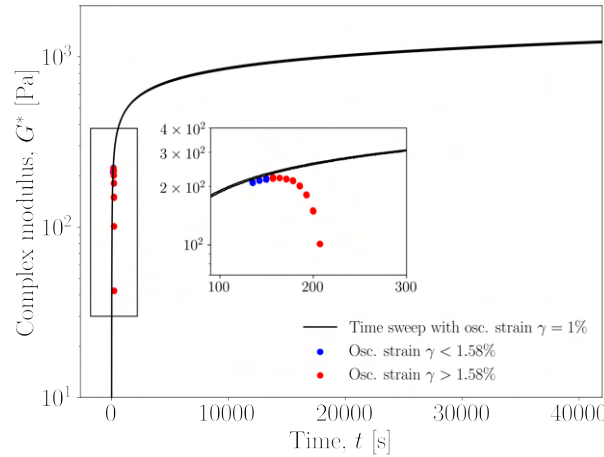
Figure 2.4: Time and amplitute sweep tests

2.3
Experimental apparatus

The experimental apparatus utilized in this work, presented in Fig. 2.7, is depicted in the schematic shown in Fig. 2.5, composed by ① pressure regulator #1, ② pressure regulator #2, ③ a pressure manometer, ④ a piston inside a steel tank, ⑤ a ball valve, ⑥ a differential pressure transducer, ⑦ the test section (i.e. the pipe with grooved walls utilized by [45]) and ⑧ a balance. The pipe has a length of 2.58 m and a nominal inner diameter of 1 cm[1]; the walls of this pipe are grooved, as shown in Fig. 2.6, in order to avoid the appearance of wall slip.

[1]As in the original publication the value of the pipe's radius $R = 4.88 \pm 0.02$ mm that furnished the best fit in a validation procedure with a newtonian oil will be utilized both in the computations regarding the pipe flow experiments and in the simulations.
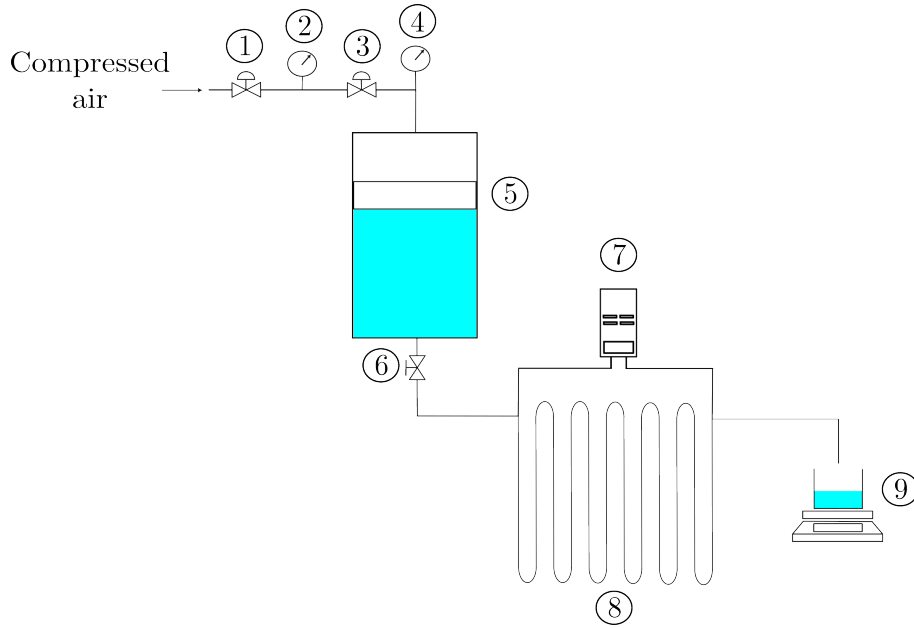
Figure 2.5: Experimental apparatus scheme
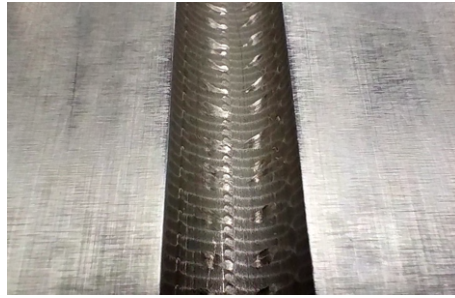
Figure 2.6: Grooved walls of the experimental apparatus' pipeline

Similarly to the rheometric experiments, a pre-test protocol was followed in order to ensure experimental repeatability and the best possible sample homogenization for the tests performed in the experimental apparatus. Initially, the fluid is poured inside the tank and mixed (i.e. pre-sheared) by an impeller equipped with a blade. The rotational velocity of the impeller was set to 470 rpm and left for 2 hours; the blade velocity was chosen according to the velocity value corresponding to rheometrical pre-test phase, corresponding to an imposed constant shear rate of 700 s^{-1}. After this pre-shear phase, the impeller is turned off and the fluidized material is quickly poured inside the pipe by opening valve ⑥ and left undisturbed for 1 hour with the valve ⑥ closed, in order to allow the material's microstructure to rebuild; this time period was chosen to be the same time waited before the onset of each rheometrical test. 5 minutes before the ending of this waiting time, the piston is placed upon the fluid level and the upper cover of the tank is coupled to the tank and the system is pressurized to a given pressure value, specified utilizing the pressure regulator ③. At the end of the waiting time, valve ⑥ is opened in order to let the fluid stored in the tank to push the fluid inside the pipeline and flow.
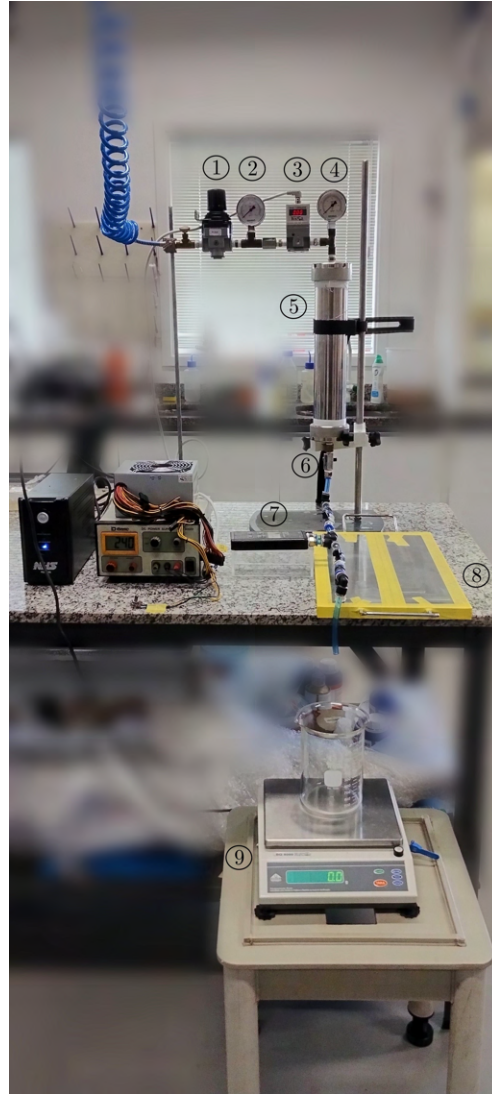
Figure 2.7: Experimental apparatus

After the flow onset, two physical variables are collected simultaneously over time: the time evolution of the mass flow rate recorded by the outgoing fluid mass collected in a beaker placed over the balance ⑨ recorded with a camera, and the pressure difference Δp obtained by the pressure transducer ⑦ value's reading. The technical specifications of the devices utilized in the experimental apparatus are presented in Tab. 2.1

Device	Accuracy	Range
Pressure transducer (Dwyer Series 490)	± 0.5 % F.S.	0-50 Psi
Pressure regulator (SMC ITV2010) ③	± 0.2 % F.S.	0-1 Bar
Balance (Gehaka BG 8000)	± 0.1 g	± 0-8 Kg

Table 2.1: Technical specifications of the devices utilized in the experimental apparatus

3
Mathematical formulation

The incompressible, isothermal and laminar flow of fluids are mathematically modelled by the continuity equation (eq. (3-1)) and the Momentum conservation equation (eq. (3-2)), where $\vec{u}$ is the velocity vector field, $\vec{g}$ the gravitational acceleration field and $\overline{\overline{T}}$ the stress tensor, defined as $\overline{\overline{T}} = -p\overline{\overline{I}} + \overline{\overline{\sigma}}$, where p is the pressure, $\overline{\overline{\sigma}}$ is the extra-stress tensor, $\overline{\overline{I}}$ and is the unit tensor.

$$\nabla \cdot \vec{u} = 0 \tag{3-1}$$

$$\rho \left(\frac{\partial \vec{u}}{\partial t} + \vec{u} \cdot \nabla \vec{u} \right) = \nabla \cdot \overline{\overline{T}} + \rho \vec{g} \tag{3-2}$$

To embed the material's rheological behavior inside the model, a constitutive equation for the extra-stress tensor that states the existent relationship between the applies shear stress and the resultant shear rate must be specified. For this work, it will be used a simplified version of the TEVP model proposed by de Souza Mendes et al. [2]; since aqueous Laponite suspensions are known to be inelastic [2, 44], viscoelastic effects will be disregarded.

3.1
The TEVP constitutive equation for the extra-stress tensor

The TEVP model proposed by [2] is composed by a differential stress equation relating $\overline{\overline{\sigma}}$ to $\overline{\overline{\dot{\gamma}}}$, where its material functions are defined to be dependent on the structural level (eq. (3-3)). In contrast to the majority of the available constitutive models in the literature, the current model specifies the structural level utilizing the dimensionless value of the fluidity, ϕ_v^* [1], defined as $\phi_v^* = (\phi_v - \phi_0)/(\phi_\infty - \phi_0)$, where ϕ_∞ is the infinite-shear rate fluidity and ϕ_0 the zero-shear rate fluidity:

$$\overline{\overline{\dot{\gamma}}} + \theta_\infty(\phi_v^*)\overset{\triangledown}{\overline{\overline{\dot{\gamma}}}} = \left[(\phi_\infty - \phi_0)\phi_v^* + \phi_0 \right] \left(\overline{\overline{\sigma}} + \theta_s(\phi_v^*)\overset{\triangledown}{\overline{\overline{\sigma}}} \right). \tag{3-3}$$

In eq. (3-3), θ_∞ is the retardation time (eq. (3-4)), θ_s the relaxation time (eq. (3-5)) and $\overset{\triangledown}{\overline{\overline{\dot{\gamma}}}}$ (eq. (3-6)) and $\overset{\triangledown}{\overline{\overline{\sigma}}}$ (eq. (3-7)) the upper-convected time derivative of the shear rate and shear stress tensors, respectively. Also, in eq. (3-4) and eq. (3-5), J is the material's compliance

$$\theta_\infty = \left(1 - \frac{\phi_v}{\phi_\infty} \right) \frac{J(\phi_v^*)}{\phi_\infty} \tag{3-4}$$

$$\theta_s = \left(1 - \frac{\phi_v}{\phi_\infty} \right) \frac{J(\phi_v^*)}{\phi_v} \tag{3-5}$$

---

[1]The fluidity is defined to be the reciprocal value of the dynamic viscosity; that is, $\phi_v = 1/\eta$

$$\overset{\triangledown}{\bar{\bar{\gamma}}} = \frac{d\bar{\bar{\gamma}}}{dt} - \bar{\bar{\gamma}} \cdot \nabla\vec{v} - \nabla\vec{v}^T \cdot \bar{\bar{\gamma}} \tag{3-6}$$

$$\overset{\triangledown}{\bar{\bar{\sigma}}} = \frac{d\bar{\bar{\sigma}}}{dt} - \bar{\bar{\sigma}} \cdot \nabla\vec{v} - \nabla\vec{v}^T \cdot \bar{\bar{\sigma}} \tag{3-7}$$

.

As previously mentioned, since elastic effects will not be considered, the material compliance will assume a null value, turning the relaxation and retardation times null. As a consequence, eq. (3-3) reduces to a Generalized Newtonian Model (eq. (3-8)).

$$\bar{\bar{\gamma}} = \left[(\phi_\infty - \phi_0)\phi_v^* + \phi_0 \right] \bar{\bar{\sigma}}. \tag{3-8}$$

Now, it must be defined how the material's structural state (i.e. ϕ_v^*) evolves over time for a given applied stress level. Eq. (3-9) will serve to this purpose, by defining the temporal rate of change of ϕ_v^* for a given applied stress level, where ϕ_{eq}^* is the steady-state value of ϕ_v^*, denominated dimensionless equilibrium fluidity. This evolution equation states that, if the material's fluidity is lower than the respective equilibrium fluidity for this stress level (i.e. $\phi_v^* < \phi_v^*(\sigma) \le \phi_{eq}^*(\sigma)$), the material will necessarily undergo a destruction process and the the temporal rate of change will be given by f_d. Equivalently, if the material's fluidity is higher than the respective equilibrium fluidity for this stress level (i.e. $\phi_{eq}^*(\sigma) < \phi_v^*(\sigma) \le 1$), the material will be undergoing a construction process, and the temporal rate of change of the dimensionless fluidity will be given by f_c.

$$\frac{\partial \phi_v^*}{\partial t} = \begin{cases} f_d(\phi_{eq}^*, \phi_v^*), & 0 < \phi_v^* \le \phi_{eq}^*; \\ f_c(\phi_{eq}^*, \phi_v^*), & \phi_{eq}^* < \phi_v^* \le 1, \end{cases} \tag{3-9}$$

As will be presented next, the functions f_d and f_c in eq. (3-9) are composed by the outputs of four rheometrical tests, namely, the creep, steady-state shear flow, construction and destruction experiment, given by eq. (3-9).

3.2
Pressure-driven flow of fluids in pipelines

For the case of the 1D pressure-driven flow inside a cylindrical pipe of radius R, where r and z are the radial and axial directions, by applying eq. (3-8) to eq. (3-2) and performing its respective dimensional simplifications, the equation of momentum conservation reduces to eq. (3-10). In this equation, it is assumed that the transient characteristic of the flow comes exclusively from the microstructural evolution of the material.

$$\frac{du_z}{dr} = \frac{1}{2}\frac{dp}{dz}r\left[\phi_v^*(\phi_\infty - \phi_0) + \phi_0\right] \tag{3-10}$$

Furthermore, to close the boundary value problem relative to eq. (3-10), the following boundary conditions are imposed: symmetry over the pipe axis, $\frac{du_z}{dr} = 0$ in $r = 0$, and the no slip condition at the pipe wall, $u_z = 0$ in $r = R$. All informations concerning the spatial domain are resumed in Fig. 3.1.
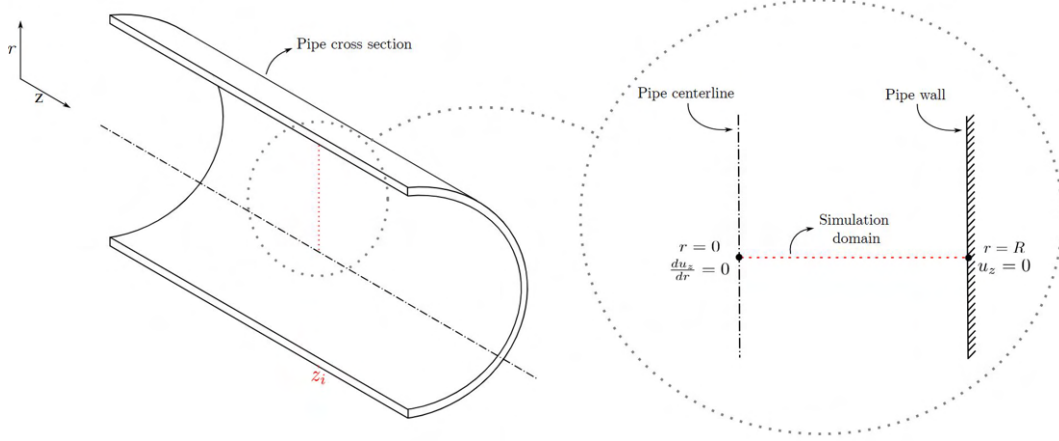
Figure 3.1: Representation of the spatial domain

In this work, it will be used the same non-dimensionalization process utilized in [1], as will be defined next and resumed in Table 3.1.

Symbol	Equation
u_z^*	$u_z \tau_c / R$
σ_R^*	$= \frac{\partial p}{\partial z} \frac{R}{2\sigma_y}$
r^*	$= \frac{r}{R}$
t_a^*	$= \frac{t_a}{\tau_c}$
τ_c	$= 1/[\sigma_y(\phi_\infty - \phi_0)])$
ϕ_{eq}^*	Eq. (3-12)
t^*	$= \frac{t}{\tau_c}$
σ^*	$= \sigma_R^* r^*$
$\dot\gamma_1^*$	$= \tau_c (\sigma_y/K)^{1/n}$
Pl	$1/\left|\sigma_R^*\right|$

Table 3.1: Dimensionless analysis utilized by de Souza Mendes et Al. [1]

In Tab. 3.1, terms with an asterisk represent the dimensionless versions of quantities represented with symbols without asterisk. $\dot\gamma_1 = (\sigma_y/K)^{1/n}$ represents the shear rate at which the transition happens from the Newtonian plateau at low shear rates to the power-law region [62], $\tau_c = 1/[\sigma_y(\phi_\infty - \phi_0)]$ a characteristic time scale [1] and $\sigma_R = \frac{\partial p}{\partial z} \frac{R}{2}$ the wall shear stress. The plastic number, Pl, as presented in the literature review, represents how much plastic the material is [42], defined as the ratio between the material's static yield stress and the highest stress value in the spatial domain (in this case, the shear stress at the pipe wall).

$$\frac{du_z^*}{dr^*} = \sigma_R^* r^* (\phi_v^* + \phi_0^*) \tag{3-11}$$

$$\phi_{eq}^* = \frac{\frac{|\sigma^*-1|^{1/n}}{\sigma^*}}{\frac{1}{\dot{\gamma}_1^*} + \frac{|\sigma^*-1|^{1/n}}{\sigma^*}} \mathcal{H}(\sigma^* - 1) \qquad (3\text{-}12)$$

$$\phi_{eq}^* = \frac{\frac{|\sigma^*-1|^{1/n}}{\sigma^*}}{\frac{1}{\dot{\gamma}_1^*} + \frac{|\sigma^*-1|^{1/n}}{\sigma^*}} \mathcal{H}(\sigma^* - 1) \qquad (3\text{-}12)$$

4
Numerical procedures

During this chapter, the numerical methods utilized to obtain both the velocity and dimensionless fluidity along the pipe radius will be presented. All numerical methods and validation procedure were chosen according to the guidelines specified in the Journal of Fluids Engineering Editorial Policy Statement on the Control of Numerical Accuracy [63]. For the boundary value problem concerning the momentum conservation equation, a 2º order finite difference scheme is utilized to discretize the differential equation along the spatial domain. The initial value problem regarding the evolution equation for the dimensionless fluidity was solved utilizing a 4º order Runge-Kutta method. In order to efficiently solve the resultant system of linear equation, the Thomas algorithm is employed to take advantage of the banded configuration of its coefficient matrix.

4.1
Discretization and solution of the boundary value problem of the momentum conservation equation

In order to discretize eq. (3-11), an approximation of the value of u_z^* at the points $r^* = r_{i+1}^*$ and $r^* = r_{i-1}^*$ will be obtained trough its respective Taylor series at the nearby point $r^* = r_i^*$. So, the respective approximation of $u_z^*(r^*)$ at $r^* = r_{i+1}^*$ and $r^* = r_{i-1}^*$ are given by eq. (4-1) and (4-2), respectively,

$$u_z^*(r_{i+1}^*) = u_z^*(r_i^*) + h\frac{du_z^*}{dr^*}\bigg|_{r^*=r_i^*} + \frac{h^2}{2}\frac{d^2u_z^*}{dr^{*2}}\bigg|_{r^*=r_i^*} + O(h^2), \quad (4\text{-}1)$$

$$u_z^*(r_{i-1}^*) = u_z^*(r_i^*) - h\frac{du_z^*}{dr^*}\bigg|_{r^*=r_i^*} + \frac{h^2}{2}\frac{d^2u_z^*}{dr^{*2}}\bigg|_{r^*=r_i^*} + O(h^2), \quad (4\text{-}2)$$

where $h = r_{i+1}^* - r_i^* = r_i^* - r_{i-1}^*$ and $O(...)$ represents the order of the local truncation error. Also, according to eq. (4-2), $\frac{d^2u_z^*}{dr^{*2}}\bigg|_{r^*=r_i^*}$ is given by eq. (4-3).

$$\frac{d^2u_z^*}{dr^{*2}}\bigg|_{r^*=r_i^*} = \frac{2}{h^2}u_z^*(r_{i-1}^*) - \frac{2}{h^2}u_z^*(r_i^*) + \frac{2}{h}\frac{du_z^*}{dr^*}\bigg|_{r^*=r_i^*} + O(h^2). \quad (4\text{-}3)$$

Applying eq. (4-3) in eq. (4-2) and isolating $\frac{du_z^*}{dr^*}\bigg|_{r^*=r_i^*}$ at the left-hand-side of the equation, results in eq. (4-4):

$$\frac{du_z^*}{dr^*}\bigg|_{r^*=r_i^*} = \frac{1}{2h}u_z^*(r_{i+1}^*) - \frac{1}{2h}u_z^*(r_{i-1}^*). \quad (4\text{-}4)$$

Eq. (4-4) will be utilized to discretize the term $\frac{du_z^*}{dr^*}\bigg|_{r^*=r_i^*}$ in eq. (3-11) at the interior points of the spatial domain showed in Fig. (3.1).

For the first point in the spatial domain (i.e. for the bounary condition at the pipe's centerline) the term $\left.\frac{du_z^*}{dr^*}\right|_{r^*=r_i^*}$ is discretized utilizing a simple forward difference scheme, given by eq. (4-5):

$$\left.\frac{du_z^*}{dr^*}\right|_{r^*=r_i^*} = \frac{1}{h}u_z^*(r_{i+1}^*) - \frac{1}{h}u_z^*(r_i^*) + O(h). \tag{4-5}$$

Since the value of the dimensionless velocity is known at the pipe wall due to the no-slip assumption, its value is simply included in the system of equation by stating that $u_z^*(r_i^*) = 0$ at the point $r_i^* = 1$, that will be represented by R^*.

In resume, the discretization of eq. (3-11) is defined by eq. (4-6), (4-7) and (4-8).

$$\frac{1}{h}u_z^*(r_{i+1}^*) - \frac{1}{h}u_z^*(r_i^*) = 0 \tag{4-6}$$

$$\frac{1}{2h}u_z^*(r_{i+1}^*) - \frac{1}{2h}u_z^*(r_{i-1}^*) = \sigma_R^* r_i^*(\phi_{v,i}^* + \phi_0^*) \tag{4-7}$$

$$u_z^*(R^*) = 0 \tag{4-8}$$

To solve the resulting set of linear equations, the Thomas algorithm, as defined in Versteeg and Malalasekera [64], is utilized. The system of equations is arranged according to eq. (4-9),

$$-\beta_i u_{z,i-1}^* + D_i u_{z,i}^* - \alpha_i u_{z,i+1}^* = c_i. \tag{4-9}$$

The values of A_i and C_i' are computed using eq. (4-10) and (4-11), respectively.

$$A_i = \frac{\alpha_i}{D_i - \beta_i A_{i-1}} \tag{4-10}$$

$$C_i' = \frac{\beta_i C_{i-1}' + c_i}{D_i - \beta_i A_{i-1}} \tag{4-11}$$

Finally, the values of $u_{z,i}^*$ are computed using eq. (4-12).

$$u_{z,i}^* = A_i u_{z,i+1}^* + C_i' \tag{4-12}$$

4.2
Solution of the initial value problem of the evolution equation for the dimensionless fluidity

In eq. (4-13) to (4-18) is defined the 4º orderd Runge-Kutta method utilized to solve the initial value problem defined by eq. (3-9) and the initial condition $\phi_{v,0}^* = 0$ [1], where f is given by eq. (3-9), $\Delta t^* = t_i - t_{i-1}$ and the order of local truncation error is of 4th order (i.e. $O(\Delta t^{*4})$). Knowing that the numerical solution of the problem is performed over the dimensionless pipe radius, both values of $\phi_{v,0}^*$ and

---

[1]The value $\phi_{v,0}^* = 10^{-8}$, instead of $\phi_{v,0}^* = 0$, was utilized for the initial condition, since the initial dimensionless fluidity being null would unable the numerical calculations for the chosen method.

$\phi_{v,i}^*$ represent the dimensionless fluidity field along this domain for the instant $t^* = t_0^*$ (for the case of $\phi_{v,0}^*$) and for $t^* = t_i^*$ (for the case of $\phi_{v,i}^*$), where the superscripts $(1), (2), ..., (R^*)$ refers to the position along the spatial domain and the subscript i refers to the temporal domain.

$$
\begin{bmatrix} \phi_{v,0}^{*(1)} \\ \phi_{v,0}^{*(2)} \\ \vdots \\ \phi_{v,0}^{*(R^*)} \end{bmatrix} = \begin{bmatrix} \phi_0^{*(1)} \\ \phi_0^{*(2)} \\ \vdots \\ \phi_0^{*(R^*)} \end{bmatrix}
\tag{4-13}
$$

$$
K_1 = \Delta t^* f \left(\begin{bmatrix} \phi_{v,i-1}^{*(1)} \\ \phi_{v,i-1}^{*(2)} \\ \vdots \\ \phi_{v,i-1}^{*(R^*)} \end{bmatrix} + \frac{\Delta t^*}{2} f \left(\begin{bmatrix} \phi_{v,i-1}^{*(1)} \\ \phi_{v,i-1}^{*(2)} \\ \vdots \\ \phi_{v,i-1}^{*(R^*)} \end{bmatrix} \right) \right)
\tag{4-14}
$$

$$
K_2 = \Delta t^* f \left(\begin{bmatrix} \phi_{v,i-1}^{*(1)} \\ \phi_{v,i-1}^{*(2)} \\ \vdots \\ \phi_{v,i-1}^{*(R^*)} \end{bmatrix} + \frac{K_1}{2} \right);
\tag{4-15}
$$

$$
K_3 = \Delta t^* f \left(\begin{bmatrix} \phi_{v,i-1}^{*(1)} \\ \phi_{v,i-1}^{*(2)} \\ \vdots \\ \phi_{v,i-1}^{*(R^*)} \end{bmatrix} + \frac{K_2}{2} \right);
\tag{4-16}
$$

$$
K_4 = \Delta t^* f \left(\begin{bmatrix} \phi_{v,i-1}^{*(1)} \\ \phi_{v,i-1}^{*(2)} \\ \vdots \\ \phi_{v,i-1}^{*(R^*)} \end{bmatrix} + K_3 \right);
\tag{4-17}
$$

$$
\begin{bmatrix} \phi_{v,i}^{*(1)} \\ \phi_{v,i}^{*(2)} \\ \vdots \\ \phi_{v,i}^{*(R^*)} \end{bmatrix} = \begin{bmatrix} \phi_{v,i-1}^{*(1)} \\ \phi_{v,i-1}^{*(2)} \\ \vdots \\ \phi_{v,i-1}^{*(R^*)} \end{bmatrix} + \frac{1}{6} \left(K_1 + 2K_2 + 2K_3 + K_4 \right)
\tag{4-18}
$$

4.3
Convergence analysis and estimation of the discretization error

In order to evaluate the error involved in the discretization of the mathematical model, the sensitivity of its output to three different sizes of mesh will be performed, both in space and time. The dimensionless average velocity at the last temporal

instant of the simulations, defined in eq. (4-22), will be utilized to perform this mesh sensitivity studies, $\bar{u}_z^*$. The evolution equation for the dimensionless fluidity of the Laponite suspension 2% wt obtained by [2] will be utilized for the simulations in this section, defined by eq. (4-19), (4-20) and (4-21) and the physical quantities of Tab. 4.1; the remaining dimensionless terms are the same as those found in Tab. 3.1.

$$\frac{\partial \phi_v^*}{\partial t^*} = \begin{cases} \frac{s}{t_a^*} \frac{(\phi_{eq}^* - \phi_v^*)^{\frac{s+1}{s}} (\phi_v^* + \phi_0^*)^{\frac{s-1}{s}}}{(\phi_{eq}^* + \phi_0^*)}, & 0 < \phi_v^* \le \phi_{eq}^*; \\ -\frac{\phi_v^* - \phi_{eq}^*}{t_c^*}, & \phi_{eq}^* < \phi_v^* \le 1 \end{cases} \tag{4-19}$$

$$t_a = 59.2 \frac{(1 - \phi_{eq}^*)^{1.1}}{(\phi_{eq}^*)^{0.4}} \tag{4-20}$$

$$t_c^* = \begin{cases} 10^4, & \phi_{eq}^* = 0; \\ 10^5, & \phi_{eq}^* > 0 \end{cases} \tag{4-21}$$

Quantity	Value
$\phi_0 \ [(Pa \cdot s)^{-1}]$	0
$\phi_\infty \ [(Pa \cdot s)^{-1}]$	64.1
$K \ [Pa \cdot s^n]$	1
$\sigma_y \ [Pa]$	6
n	0.32

Table 4.1: Values of the physical quantities for the 2 % obtained in [2]

With regard to the discretization of the time domain, as can be noticed in Tab. 4.3, for dimensionless time steps lower than $\Delta t^* \approx 7.19$, the difference between the values of $\bar{u}_z^*$ for finer meshes is negligible, which indicates that $\Delta t^* \approx 7.19$ is an appropriate choice for Δt^{*2}.

To obtain the spatial apparent order of convergence of the numerical procedure and estimate its related distretization error, the procedure proposed in Celik et Al. [63], as presented in the five-step process described below, will be utilized. For this convergence analysis, it was set that $s = 15$ and $Pl = 0.05$.

$$\bar{u}_z^* = 2 \int_0^1 u_z^*(r^*) r^* dr^* \tag{4-22}$$

1. A spatial quantity relative to the level of discretization, that henceforth will be denoted by l, must be chosen. Since the velocity profile varies only in one dimension, the only option left is to utilize h as defined in sec. 4.1.

$$\beta_{32} = \frac{l_3}{l_2}; \ \beta_{21} = \frac{l_2}{l_1} \tag{4-23}$$

2. Perform three simulations with three different grid element size and compute its respective variable of interest, ϕ, for each simulation; the corresponding

---

[2]For all simulations performed for this analysis, Δr^* of the fine mesh in Tab. 4.2 was utilized

	$\Delta r*$	$\bar{u}_z^*$
Coarse	0.006711409395973164	4.964581068210729
Medium	0.002004008016032	4.964759782369221
Fine	0.0012515644555694677	4.964771753701966

Table 4.2: Sensitivity analysis of the dimensionless radius step size to the value of $\bar{u}_z^*$

	$\Delta t*$	$\bar{u}_z^*$
Coarse	2.8572244921233505	4.964771752026877
Medium	2	4.964771753701966
Fine	1	4.9647717661493305

Table 4.3: Sensitivity analysis of the dimensionless time step size to the value of $\bar{u}_z^*$

value of l for each simulation will be called l_{coarse} referring to the simulation with the coarsest mesh, l_{medium} or l_{fine} for simulations using an intermediate and fine mesh, respectively. Also the grid refinement factor is defined as $\beta = l_{\text{coarser}}/l_{\text{finer}}$; in the original publication, the authors suggests that values of l that return β greater than 1.3 must be chosen. So, Considering that the numbers 1, 2 and 3 will denote the fine, medium and coarse mesh simulations, respectively, the values of β for the coarse and medium, β_{32}, and medium and fine simulations, β_{21}, are defined as $\beta_{32} = \frac{l_3}{l_2}$ and $\beta_{21} = \frac{l_2}{l_1}$; the values of the difference between the variable of interest, obtained for the coarse and medium mesh, ϵ_{32}, and for the medium and fine mesh, ϵ_{21}, are defined as $\epsilon_{32} = \phi_3 - \phi_2$ and $\epsilon_{21} = \phi_2 - \phi_1$. Also, the parameter s is defined in eq. (4-24).

$$s = \begin{cases} 1, & \epsilon_{32}/\epsilon_{21} > 0 \\ -1, & \epsilon_{32}/\epsilon_{21} < 0 \end{cases} \tag{4-24}$$

3. Compute the apparent order of convergence of the numerical method, p, by solving eq. (4-25):

$$p = \frac{1}{ln(\beta_{21})} \left| ln |\epsilon_{32}/\epsilon_{21}| + ln \left(\frac{\beta_{21}^p - s}{\beta_{32}^p - s} \right) \right|, \tag{4-25}$$

4. Calculate ϕ_{ext}^{21} as defined in eq. (4-26).

$$\phi_{\text{ext}}^{21} = \frac{\beta_{21}^p \phi_1 - \phi_2}{\beta_{21}^p - 1} \tag{4-26}$$

5. Calculate the approximate relative error, eq. (4-27), the extrapolated relative error, eq. (4-28), and the fine-grid convergence index, eq. (4-29).

$$e_a^{21} = \left| \frac{\phi_1 - \phi_2}{\phi_1} \right| \tag{4-27}$$

$$e_{ext}^{21} = \left| \frac{\phi_{ext}^{21} - \phi_1}{\phi_{ext}^{21}} \right| \qquad (4\text{-}28)$$

$$GCI_{\text{fine}}^{21} = \frac{1.25 e_a^{21}}{\beta_{21}^p - 1} \qquad (4\text{-}29)$$

e_a^{21} [%]	e_{ext}^{21} [%]	GCI_{fine}^{21} [%]	p	ϕ_{ext}^{21}
0.000241	0.000168	0.00021	1.89	4.964780116432123

Table 4.4: Results of the spatial convergence analysis and the estimation of its discretization error

In Tab. 4.4, e_a^{21} is the relative error between ϕ_1 and ϕ_2, e_{ext}^{21} the relative error between ϕ_1 and the theoretical value of ϕ computed utilizing a Δr^* value that approaches zero (ϕ_{ext}^{21}), p the order of convergence of the numerical method and GCI_{fine}^{21} a numerical quantity that offers a geometric insight into how numerical inaccuracies change as the grid size vary.

The results for the spatial convergence analysis and the estimation of its respective discretization error is given in Tab. 4.4. In view of the obtained results, from now on, the Δr^* value corresponding to the fine mesh (see Tab. 4.2) and Δt^* value corresponding to the medium mesh (see Tab. 4.3) will be utilized for every simulation.

5
Results and Discussion

In this chapter, an evolution equation for the dimensionless fluidity of the Laponite suspension presented in sec. 2.1 is obtained following the framework proposed by de Souza Mendes et Al. [2]. Next, the influence of thixotropy in pressure-driven restart processes will be presented for two fluids. The first fluid is the Laponite suspension 1.25 % wt (denominated "Fluid A") obtained in sec. 5.1. The second one is the model for a Laponite suspension 2% wt (denominated "Fluid B") reported in [2] that was utilized in sec. 4.3. The analysis of the impact of thixotropy in the flow restart consisted in comparing how these materials with different thixotropic responses behaved in the process; the simulations were performed for different combinations of *Pl* and *s* for each fluid. Furthermore, an attempt to evaluate the prediction capability of the model for Fluid A was made by comparing the results from the simulations and the results obtained utilizing the experimental apparatus presented in sec. 2.3.

5.1
Evolution equation for the dimensionless fluidity of the Laponite suspension 1.25 % wt presented in chapter 2.1

First, the Laponite suspension's static yield stress is determined through a series of creep tests. This experimental procedure consists in impose a constant shear stress value to the material in its totally structured state and then monitoring the shear rate output. For creep tests where the output falls to negligible values of shear rate during the test period, it will be considered that the applied shear stress is lower than the material's static yield stress, once it is incapable of promote a microstructural breakdown. Otherwise, if the test's output registers a dramatic increase in the shear rate and the sample starts to get progressively fluidized, the applied shear stress will be considered to be higher than the static yield stress. In Fig. 5.1 it is shown the output of the performed tests for three different values of applied shear stress.

From Fig. 5.1 it can be clearly noticed that for stress values higher than 13 Pa exists a transition in the qualitative behavior of the shear rate's response, where at a given point in time occurs an irreversible yield. So, the static yield stress will be computed as the simple average of the minimum stress able to fluidize the sample (i.e. 13 Pa) and the one right below it (i.e. 12 Pa). So, the computed static yield stress has a value of 12.5 Pa.

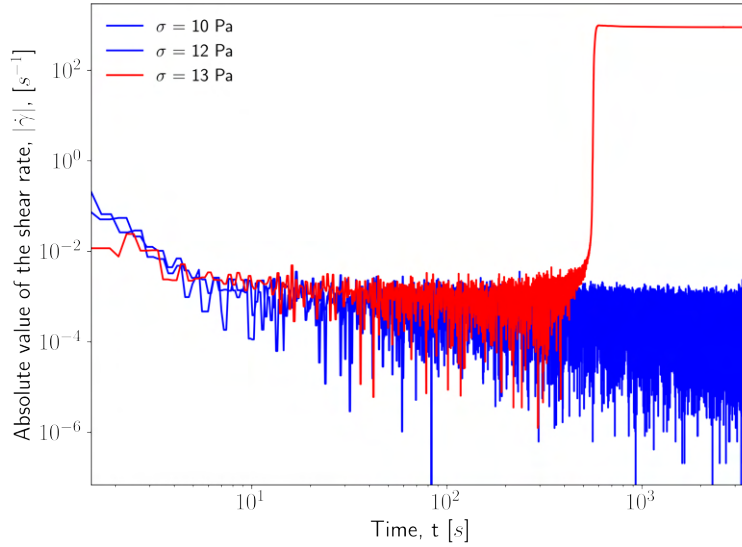The equilibrium values of the fluidity are obtained through a common

Figure 5.1: Creep test output

experimental procedure dedicated in obtain the material's flow curve in a ramp-down shear-rate controlled test configuration. The data aquisition was set to five points per decade in a set of shear-rate values in log scale, where the steady-state criterion was defined to 3 consecutive computations of the averaged output value within 30 s, with a tolerance of 0.5 %, within a maximum time of test of 1800 s; the experimental data was obtained in terms of the kinematic viscosity, η. Subsequently, the correspondent values of fluidity (i.e. $\phi_v = 1/\eta$) were computed and fitted to eq. 5-1. Finally, the results are expressed in terms of the dimensionless fluidity (eq. 5-2) and shown in Fig. 5.2. For tests with shear-rate values lower than $900 s^{-1}$, the grooved geometry was used, in order to exclude the hypothesis of the test output be influenced by the wall slip phenomenon. Whilst, for tests with shear-rate value higher than $900 s^{-1}$ the geometry with smooth surfaces was used, in order to avoid the formation of secondary flow during the tests.

$$\phi_{eq}(\sigma) = \phi_0 + \frac{(\phi_\infty - \phi_0)\left[\frac{1}{\sigma}\left(\frac{|\sigma - \sigma_y|}{K}\right)^{1/n}\right]}{(\phi_\infty - \phi_0) + \left[\frac{1}{\sigma}\left(\frac{|\sigma - \sigma_y|}{K}\right)^{1/n}\right]}\mathcal{H}(\sigma - \sigma_y) \tag{5-1}$$

$$\phi_{eq}^*(\sigma) = \frac{\left[\frac{1}{\sigma}\left(\frac{|\sigma - \sigma_y|}{K}\right)^{1/n}\right]}{(\phi_\infty - \phi_0) + \left[\frac{1}{\sigma}\left(\frac{|\sigma - \sigma_y|}{K}\right)^{1/n}\right]}\mathcal{H}(\sigma - \sigma_y) \tag{5-2}$$

The function f_d in eq. (3-9) was obtained by a series of fitted outputs of destruction tests. These tests comprises in initially impose a constant shear stress lower than the static yield stress to the sample and, when steady-state is achieved, a shear stress value step change is applied, with a shear stress value higher than the static yield stress. The test's output is the temporal shear-rate evolution that will be
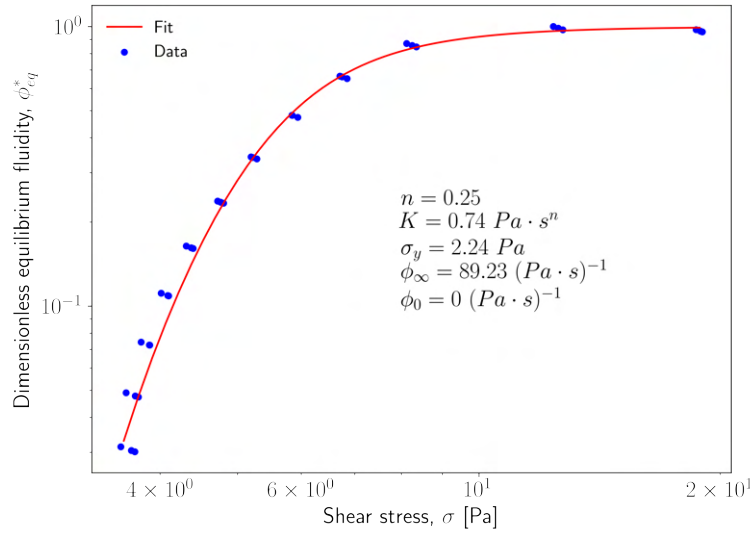
Figure 5.2: Steady-state's test output

posteriorly fitted to eq. (5-3), aiming to obtain the values of t_a and s , which are the avalanche time and a parameter that measure the recklesness of the material's breakage.

$$\phi_\nu^*(t) = \phi_{eq}^* \frac{t^s}{t_a^s + t^s} \tag{5-3}$$

From Fig. 5.3 to Fig. 5.7 are shown the destruction test's output. For each case, two tests for each final stress value were performed to check the experimental repeatability; in every case, excellent results were obtained. By analysing the dimensionless fluidity steady-state value reported in Fig. 5.2. knowing that the material's static yield stress have a value of 12.5 Pa, it is noticed that only a small parcel of the curve represented in Fig. 5.2 will be available for a material restarting to flow from its fully-structuced state. Also, the attainable equilibrium structural states pertain to a correspondent shear-rate values range where secondary flows are expected to appear if the geometry with grooved surfaces is used. Since it was the case, secondary flows were present in all tests; this fact can be noticed by analysing the shear-rate response of the tests: it is perceived that as higher values of stress are applied, the equilibrium value of the dimensionless fluidity decreases. Such response is clearly unphysical, since it contrasts with the extensively observed one-to-one relationship between σ and $\dot{\gamma}$ available in the literature. So, only the output relative to a shear-rate maximum of 900 s^{-1} was used to realize all curve fitting procedures. In all figures presenting the destruction test data are showed both the test's output and the function correspondent to the fitting procedure. It is important to highlight that these functions assume the respective equilibrium value furnished by the equilibrium curve for the given applied stress.
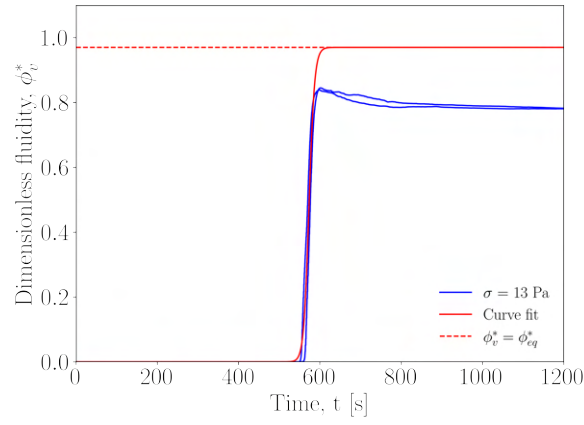
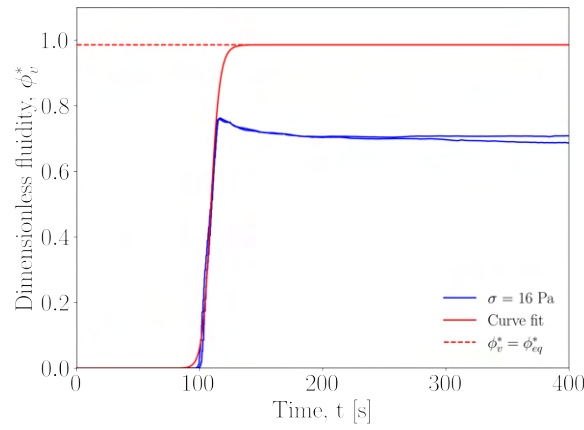Figure 5.3: Destruction test for σ = 13 Pa; t_a = 573.5 and s = 86.5

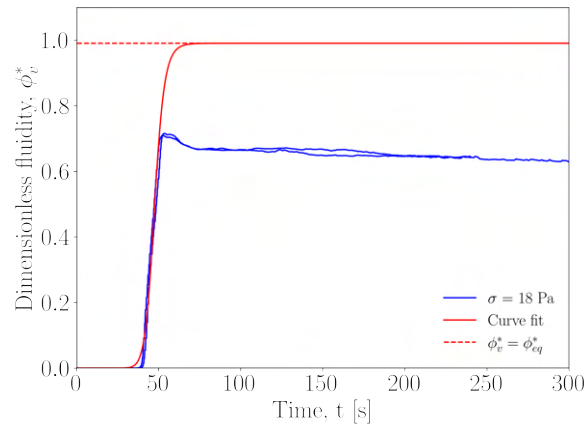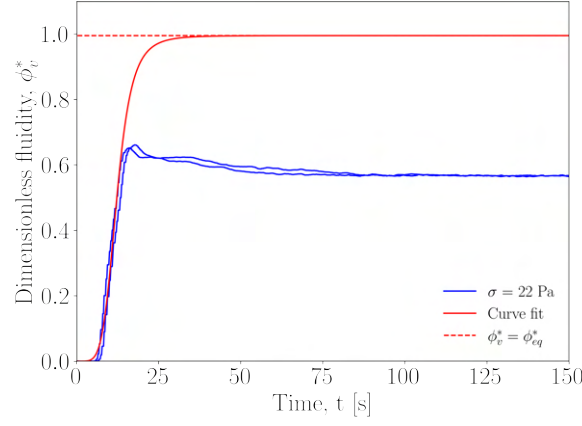Figure 5.4: Destruction test for σ = 16 Pa; t_a = 109.1 and s = 30.7

Figure 5.5: Destruction test for σ = 18 Pa; t_a = 47.5 and s = 15.8

Figure 5.6: Destruction test for $\sigma = 22$ Pa; $t_a = 12.2$ and $s = 5.2$
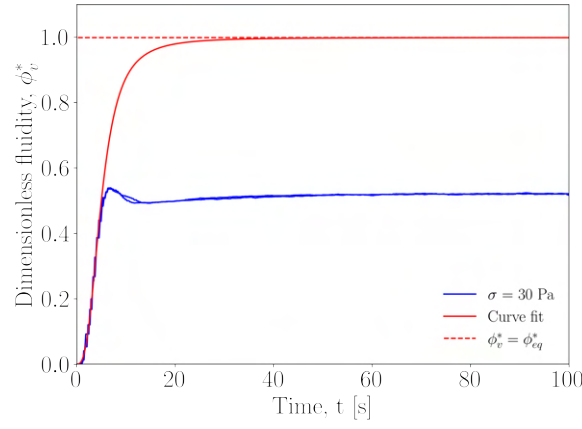
Figure 5.7: Destruction test for $\sigma = 30$ Pa; $t_a = 5.03$ and $s = 2.8$

With the values of t_a and s at hand, both quantities can be fitted to appropriate functions, with respect to the shear stress level. Eq. (5-4) and eq. (5-5) are used to fit the t_a and s data, respectively. Since processes where exist reconstruction of the microstructure will not be studied, the function f_c in eq. (3-9) will not be determined.

$$t_a(\phi_{eq}^*) = a\frac{(1 - \phi_{eq}^*)^b}{\phi_{eq}^{*c}} \tag{5-4}$$

$$s(\phi_{eq}^*) = a - \frac{b}{\left[1 + \left(\phi_{eq}^* c\right)^d\right]^e} \tag{5-5}$$

Finally, eq. (5-6) can be applied in eq. (3-9) and the temporal rate of change of the dimensionless fluidity is defined (eq. (5-7)).

$$f(\phi_{eq}^*, \phi_v^*) = \frac{s}{t_a \phi_{eq}^*} \left(\phi_{eq}^* - \phi_v^*\right)^{\frac{s+1}{s}} \phi_v^{*\frac{s-1}{s}} \tag{5-6}$$

$$\frac{\partial \phi_v^*}{\partial t} = \frac{s}{t_a \phi_{eq}^*} \left(\phi_{eq}^* - \phi_v^*\right)^{\frac{s+1}{s}} \phi_v^{*\frac{s-1}{s}} \tag{5-7}$$
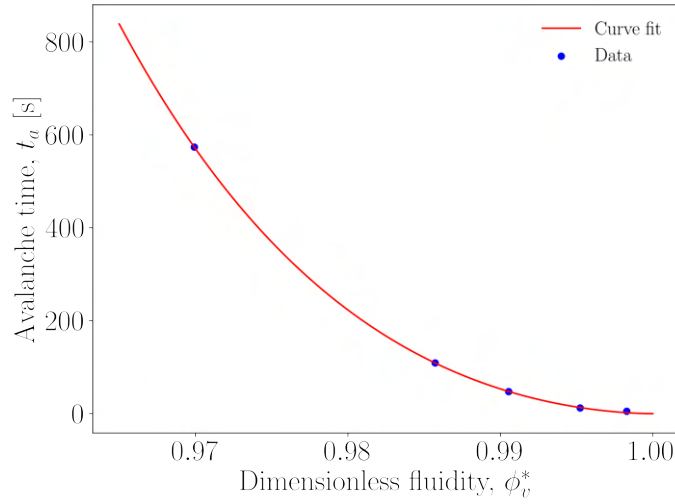
Figure 5.8: Curve fit for t_a data obtained from the destruction experiments; $a = 1.2 \cdot 10^5$, $b = 1.7$ and $c = 2.3 \cdot 10^1$.
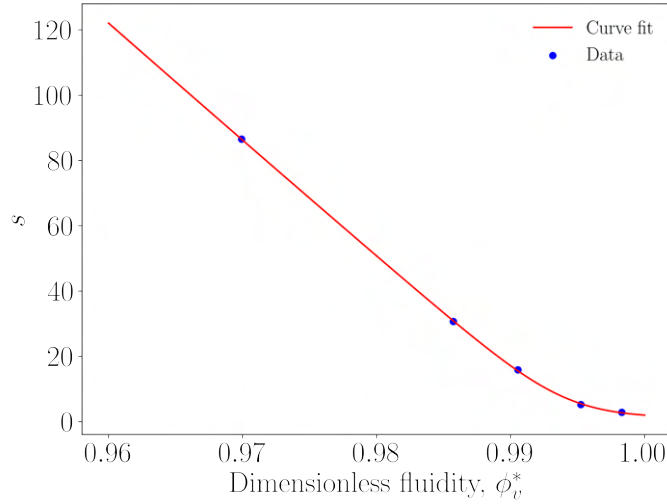
Figure 5.9: Curve fit for s data obtained from the destruction experiments; $a = 1.2 \cdot 10^5$, $b = 1.2 \cdot 10^5$, $c = 1.006$, $d = -3.989 \cdot 10^2$ and $e = 7.2 \cdot 10^{-5}$.

5.2
Simulations with application of a constant pressure gradient

From Fig. 5.10a to Fig 5.10i are presented the temporal evolution of the dimensionless fluidity over the dimensionless radius of the pipeline for Fluid A and in Fig. 5.11a to Fig 5.11i its correspondent dimensionless velocity distribution. For Fluid B, the dimensionless fluidity field is presented in Fig. 5.12a to Fig. 5.12i and the dimensionless velocity fields in Fig. 5.13a to Fig. 5.13i. For both fluids, the simulations were ran for three different combinations of $Pl = [0.05, 0.12, 0.18]$ and $s = [3, 9, 15]$. Low values of Pl indicates higher pressure gradients imposed to the material, in comparison to higher values of Pl, and low values of s will represent materials more thixotropic than materials with higher values of s; it is important to notice that the parameter s in eq. (5-3) is responsible for dictating the degree of

thixotropy exhibited by the materials.

By analyzing the temporal evolution of the dimensionless fluidity for fluid A for a given *Pl*, (e. g. by observing Figs. 5.10a (*Pl* = 0.05 and *s* = 3), 5.10b (*Pl* = 0.05 and *s* = 9) and 5.10c (*Pl* = 0.05 and *s* = 15)), it is perceived that for the case with a higher level of thixotropy, *s* = 3, the fluid undergoes a more gradual evolution of its dimensionless fluidity towards an equilibrium value in each radial position, indicated by a progressive transition from a rest state (black regions) to flow (white regions), in contrast with the cases for *s* = 9 and *s* = 15 (i.e. for lower levels of thixotropy), where abrupt transitions are represented by well-demarcated regions of fully-structured (black regions) and highly unstructured (white regions) material over the dimensionless pipe radius. Also, it can be observed that the model predicts earlier flow restarts for lower values of *Pl*, i. e. for higher pressure differences applied (e. g. by observing Figs. 5.10a (*Pl* = 0.05 and *s* = 3), 5.10d (*Pl* = 0.12 and *s* = 3) and 5.10g (*Pl* = 0.18 and *s* = 3)), as expected. The same qualitative behavior is exhibited by fluid B, as can be confirmed in Fig. 5.12.

Through a visual examination of the evolution of the dimensionless velocity profiles for both fluids for a given value of *Pl* (Fig. 5.2 and Fig. 5.4), no appreciable impact of different thixotropy levels could be perceived with respect to the steady-state dimensionless velocity at the end of the simulations. In order to give a closer look to the evolution of the dimensionless velocity profile towards steady-state, in Fig. 5.14 and Fig. 5.15 are shown the time evolution for 6 different instants pertaining the dimensionless time span of the simulation for Fluid A and Fluid B, respectively. As can be clearly noticed, despite the velocity profiles for different values of *s* evolved differently over time, the same velocity profile was attained for a given value of *Pl*.

From these observations, it can be concluded that the thixotropic feature affected the qualitative behavior of the material during the transient period of the restart process, but no influence was registered in the steady-state state. As expected, lower values of Pl resulted in quicker restarts. Also, greater regions of sheared material were present for the simulations with the lowest Pl values, in comparison with the others. Unfortunately, for fluid B, it was not possible to attain a steady-state for the chosen time span, suggesting that the thixotropic feature of the material could be not the only property that influence the material's rheological development.

(a) $Pl = 0.05$ and $s = 3$

(b) $Pl = 0.05$ and $s = 9$

(c) $Pl = 0.05$ and $s = 15$

(d) $Pl = 0.12$ and $s = 3$

(e) $Pl = 0.12$ and $s = 9$

(f) $Pl = 0.12$ and $s = 15$

(g) $Pl = 0.18$ and $s = 3$

(h) $Pl = 0.18$ and $s = 9$

(i) $Pl = 0.18$ and $s = 15$
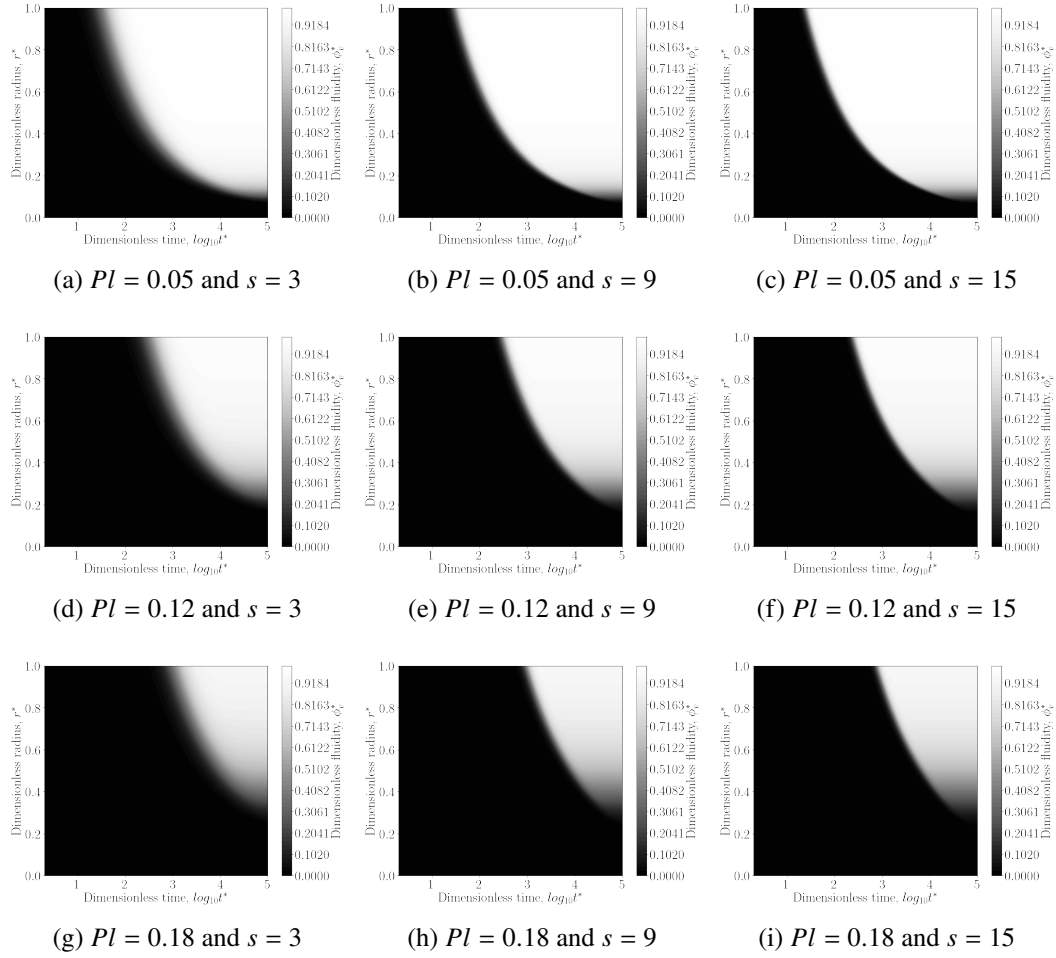
Figure 5.10: Evolution of the dimensionless fluidity field for Laponite A for different Pl and s values.

(a) *Pl* = 0.05 and *s* = 3 (b) *Pl* = 0.05 and *s* = 9 (c) *Pl* = 0.05 and *s* = 15

(d) *Pl* = 0.12 and *s* = 3 (e) *Pl* = 0.12 and *s* = 9 (f) *Pl* = 0.12 and *s* = 15

(g) *Pl* = 0.18 and *s* = 3 (h) *Pl* = 0.18 and *s* = 9 (i) *Pl* = 0.18 and *s* = 15
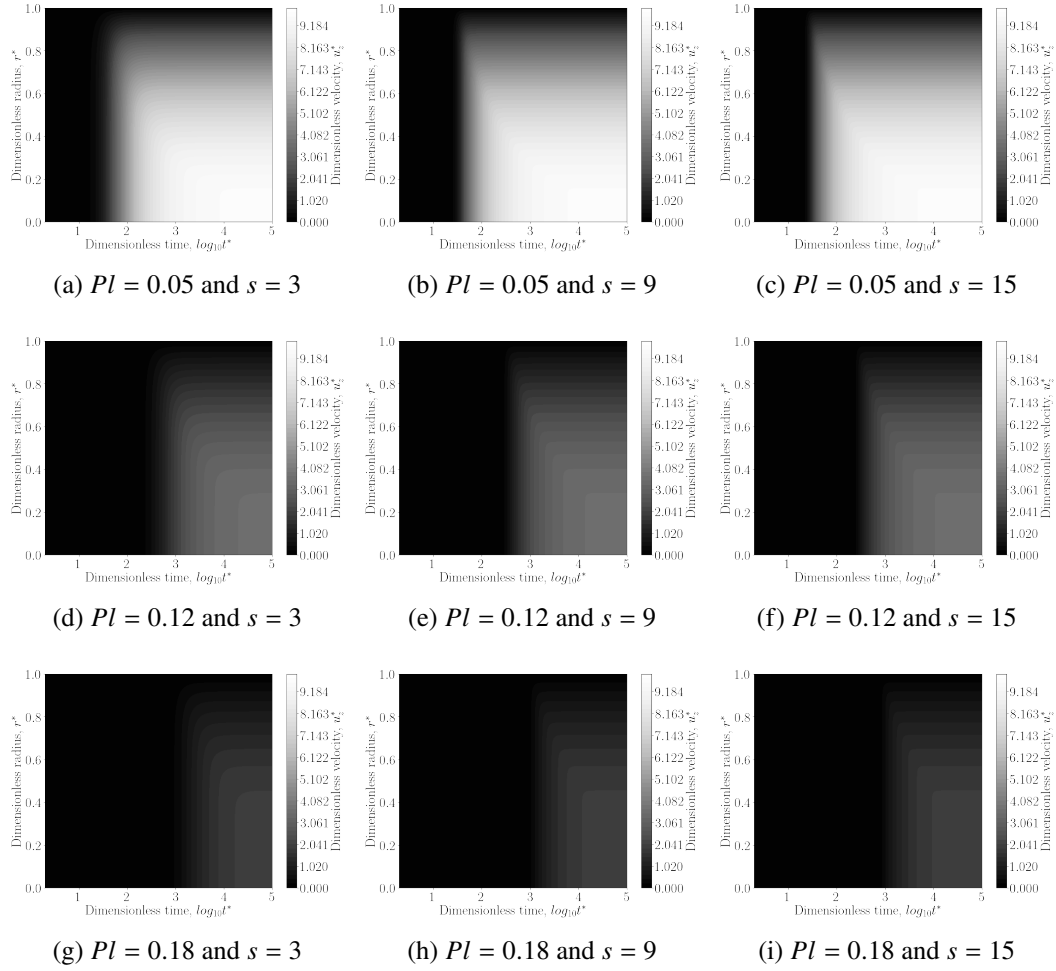
Figure 5.11: Evolution of the dimensionless velocity field for Laponite A for different *Pl* and *s* values.

(a) *Pl* = 0.05 and *s* = 3

(b) *Pl* = 0.05 and *s* = 9

(c) *Pl* = 0.05 and *s* = 15

(d) *Pl* = 0.12 and *s* = 3

(e) *Pl* = 0.12 and *s* = 9

(f) *Pl* = 0.12 and *s* = 15

(g) *Pl* = 0.18 and *s* = 3

(h) *Pl* = 0.18 and *s* = 9

(i) *Pl* = 0.18 and *s* = 15
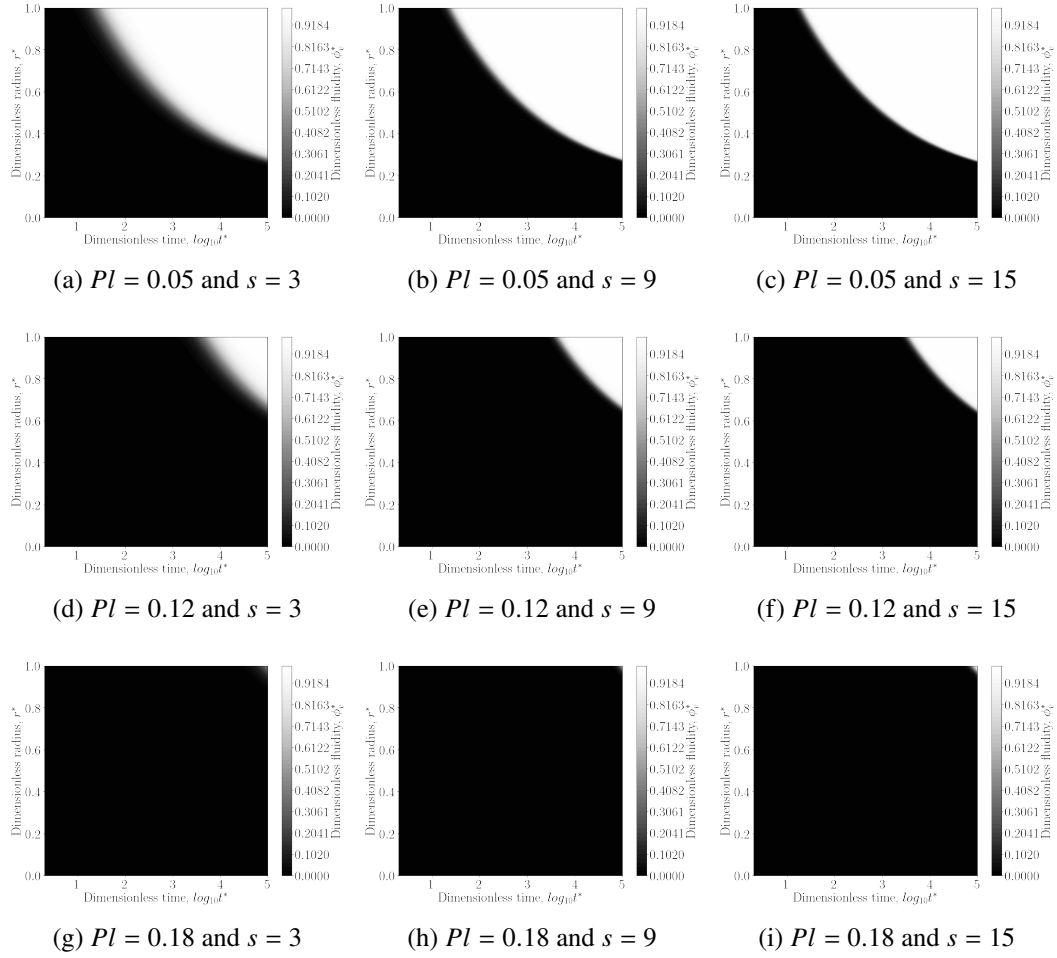
Figure 5.12: Evolution of the fluidity field for Laponite B for different *Pl* and *s* values.

(a) *Pl* = 0.05 and *s* = 3   (b) *Pl* = 0.05 and *s* = 9   (c) *Pl* = 0.05 and *s* = 15

(d) *Pl* = 0.12 and *s* = 3   (e) *Pl* = 0.12 and *s* = 9   (f) *Pl* = 0.12 and *s* = 15

(g) *Pl* = 0.18 and *s* = 3   (h) *Pl* = 0.18 and *s* = 9   (i) *Pl* = 0.18 and *s* = 15
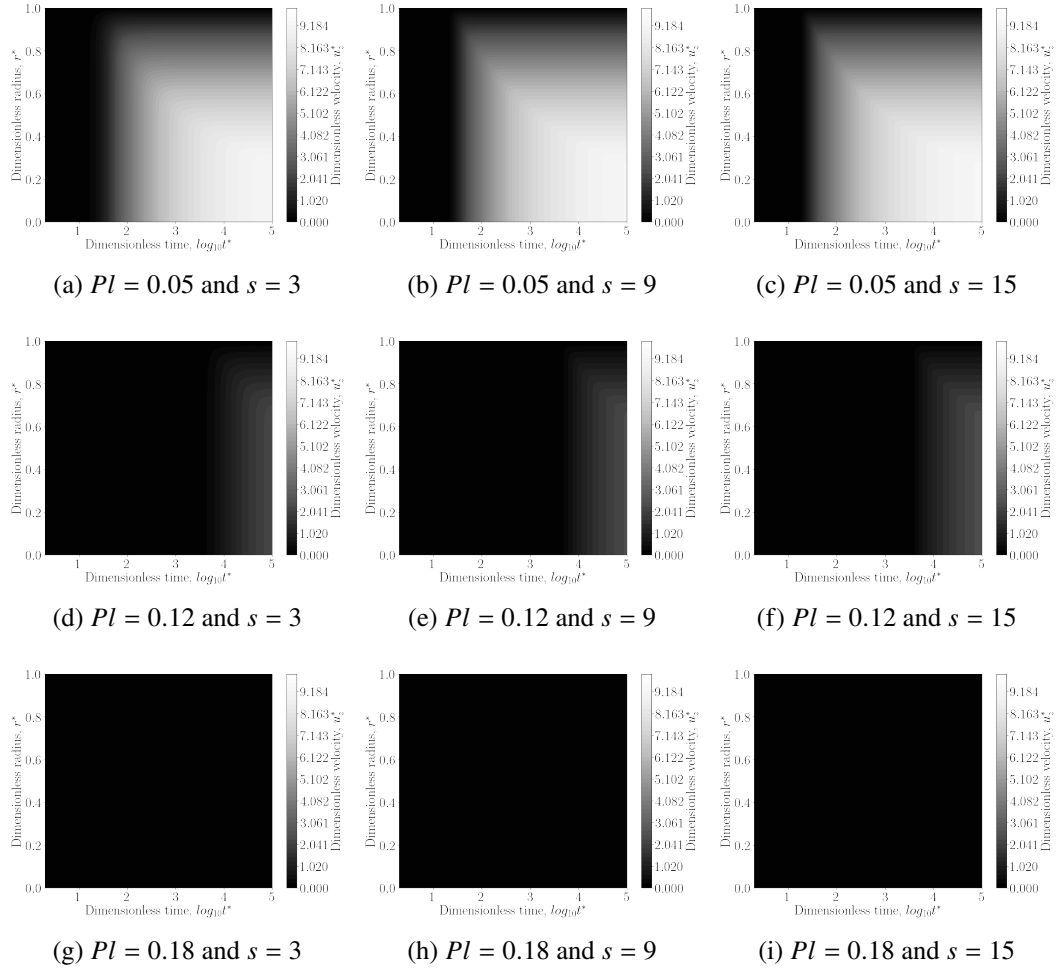
Figure 5.13: Evolution of the velocity field for Laponite B for different *Pl* and *s* values.

(a) $t^* = 50$

(b) $t^* = 100$

(c) $t^* = 700$

(d) $t^* = 4000$

(e) $t^* = 24000$

(f) $t^* = 100000$

(g) Temporal evolution of the dimensionless plug velocity.

Figure 5.14: Temporal evolution of the dimensionless velocity profile for Laponite A for $Pl = 0.05$ (solid lines), $Pl = 0.12$ (dashed lines) and $Pl = 0.18$ (dash-dot lines) (From (a) to (f)); in (g) it is represented the temporal evolution of the dimensionless plug velocity

(a) $t* = 50$

(b) $t* = 100$

(c) $t* = 700$

(d) $t* = 4000$

(e) $t* = 24000$

(f) $t^* = 100000$

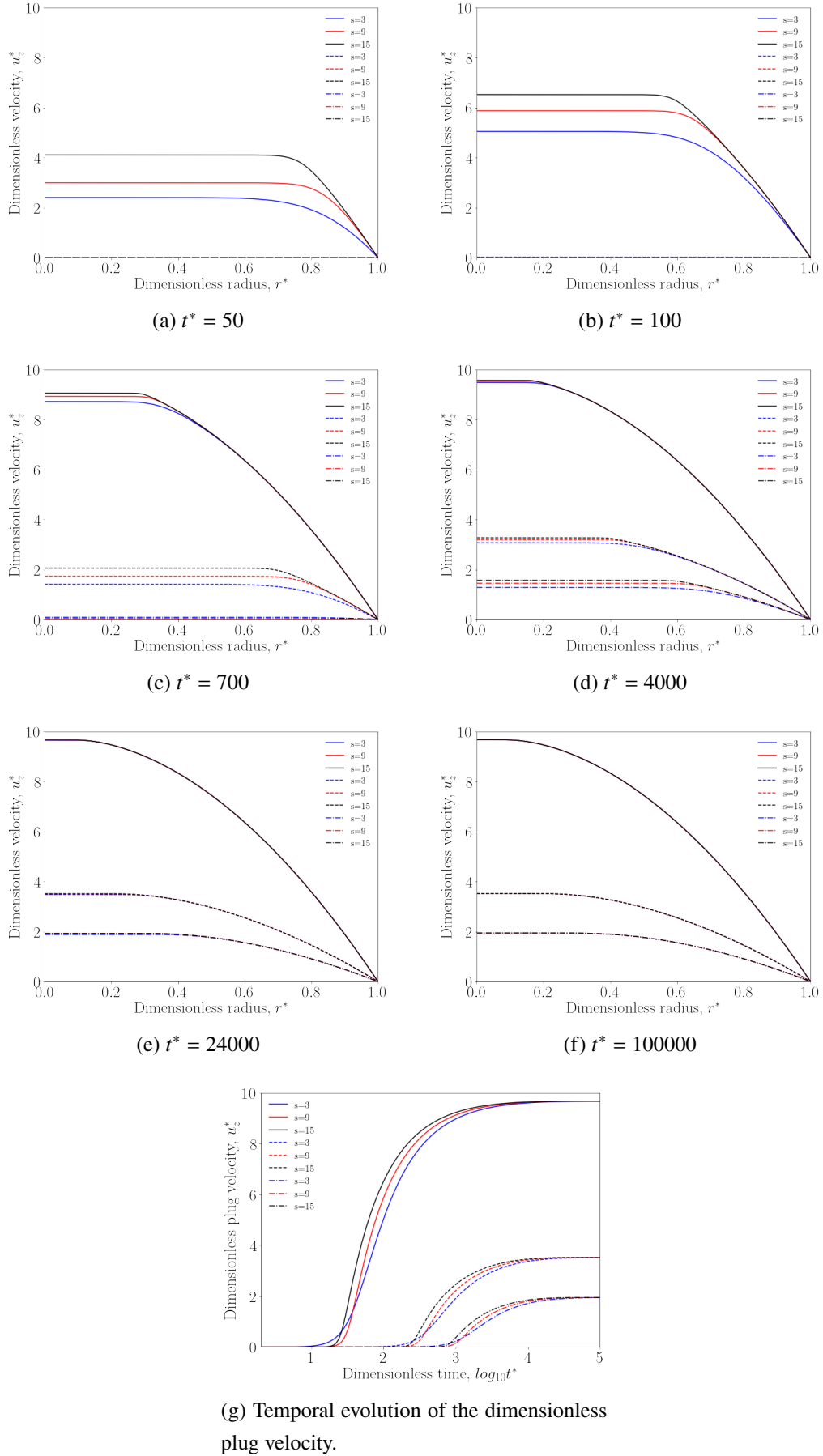(g) Temporal evolution of the dimensionless plug velocity
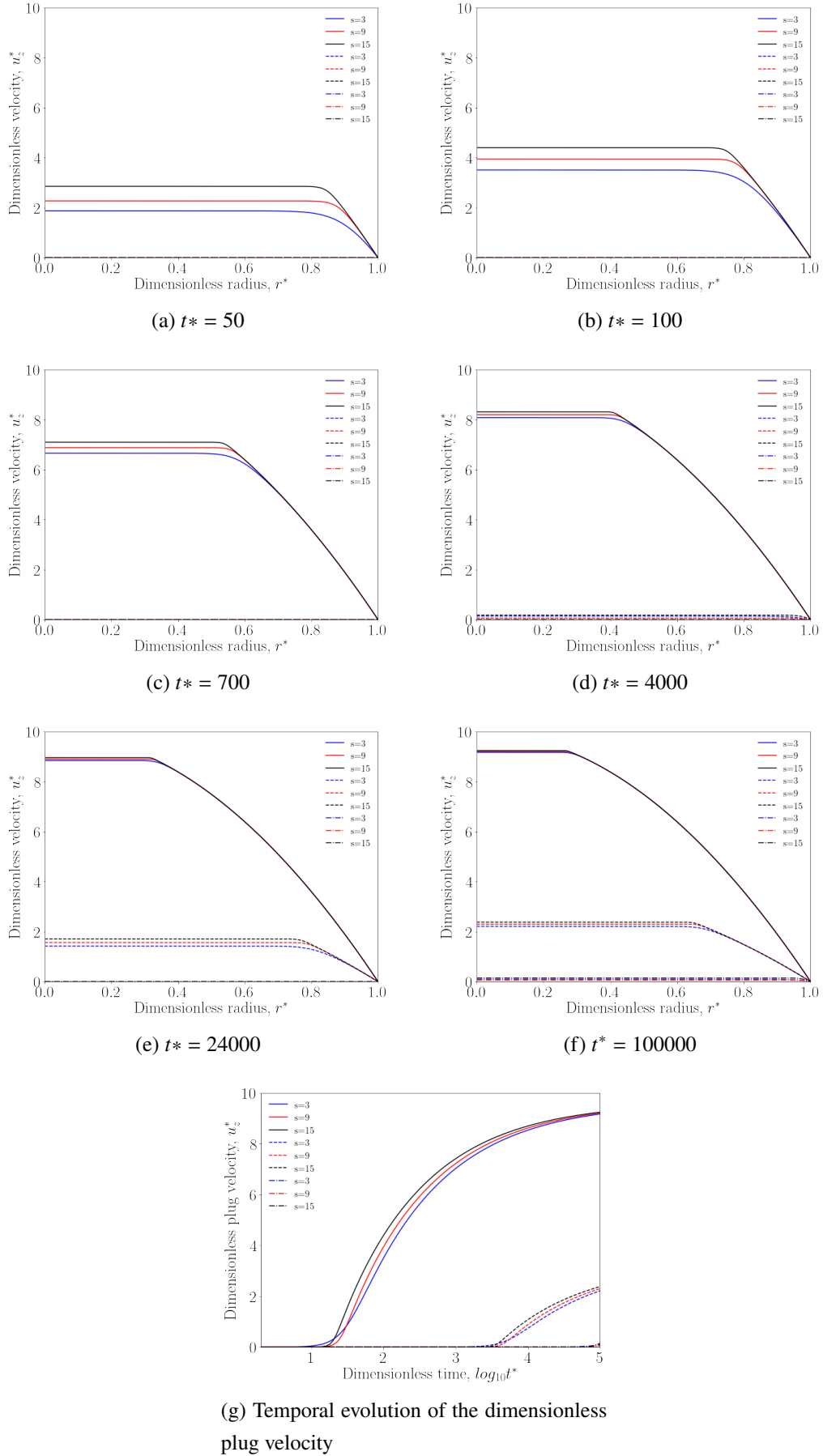
Figure 5.15: Temporal evolution of the dimensionless velocity profile for Laponite B for $Pl = 0.05$ (solid lines), $Pl = 0.12$ (dashed lines) and $Pl = 0.18$ (dash-dot lines) (From (a) to (f)); in (g) it is represented the temporal evolution of the dimensionless plug velocity

5.3
Simulation of real pipe flow experiments

The results of the experimental tests carried out on the experimental bench shown in Fig. 2.7 and their respective simulations will now be presented. Due to the small amount of material left from the rheological tests, it was possible to carry out only 4 experiments, two of them setting the pressure in the pressure regulator at 0.3 Bar and the other two at 0.4 Bar; the pressure difference values collected over time from the experiments are presented in Fig. 5.16a and 5.16b. The simulations were performed considering both t_a and s being functions of the applied stress, whose functions were obtained through rheological experiments and presented in Fig. 5.8 and Fig. 5.9, respectively.

Through Fig. 5.16a and 5.16b it is possible to see that it was not possible to maintain a constant pressure difference during all four experiments, despite having good repeatability. This result was caused by the high roughness of the cylinder walls, which prevented the piston from move freely. Given this situation, it was decided to perform a simple average of the values obtained for ΔP and consider in the simulations that the pressure was imposed constantly. The temporal evolution of the dimensionless fluidity and velocity fields are given in 5.17a and 5.17b for the case of 0.3 Bar and in Fig. 5.18a and 5.18b for the case of 0.4 Bar. A comparison between the resultant mass flow rate obtained in the experiments and the numerical predictions are presented in Fig. 5.19a and 5.20a.

As evident from Fig. 5.19a and Fig. 5.20a, there exists a significant disparity between the experimental and numerical results in both cases. This variance in outcomes could stem from several factors. Since there is no information available regarding the minimum pipe length required for flow development, possibly the short length of the pipeline may have prevented the flow to develop. Also, by failing to maintain a constant pressure within the tank and assuming that the imposed pressure difference was the arithmetic average of the pressure differences recorded throughout the test, may have led to an overestimation of the resulting mass flow rate computed numerically.

However, it is important to note that such tests were also carried out with thixotropic materials by de Souza Mendes et al. [2], which also obtained great divergence in the comparison of numerical and experimental data; unlike this work, the authors used a Herschel-bulkley model to carry out their simulations.
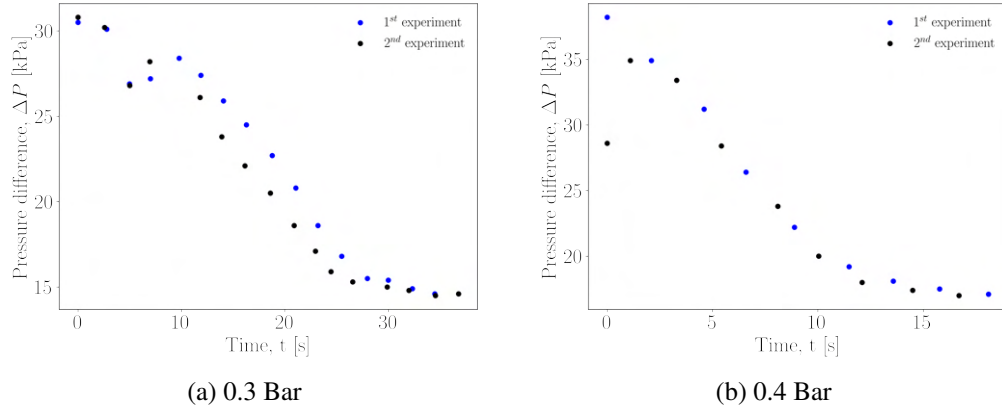
(a) 0.3 Bar

(b) 0.4 Bar

Figure 5.16: Pressure difference recorded during four restart experiments (two with 0.3 Bar and two with 0.4 Bar) in the experimental apparatus

(a) Temporal evolution of the dimensionless fluidity field

(b) Temporal evolution of the dimensionless velocity field
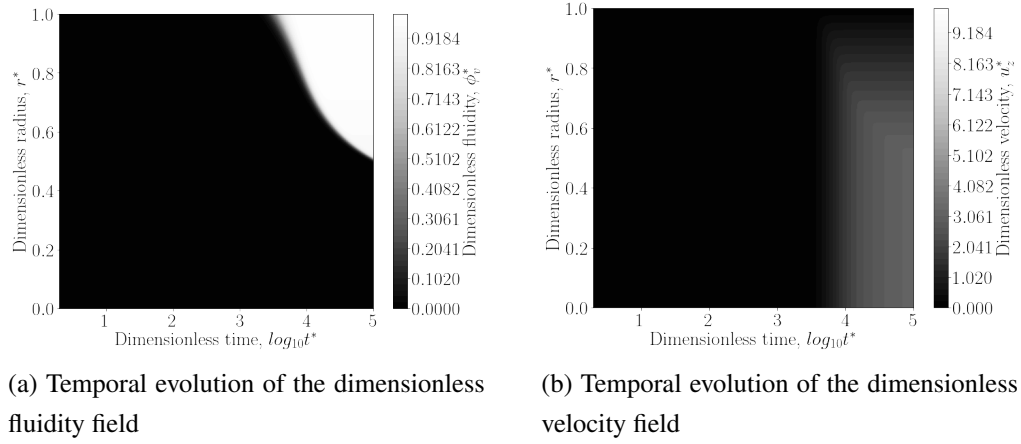
Figure 5.17: Simulation for $\frac{\Delta P}{L} = 7974.23$ Pa (0.3 Bar)

(a) Temporal evolution of the dimensionless fluidity field

(b) Temporal evolution of the dimensionless velocity field
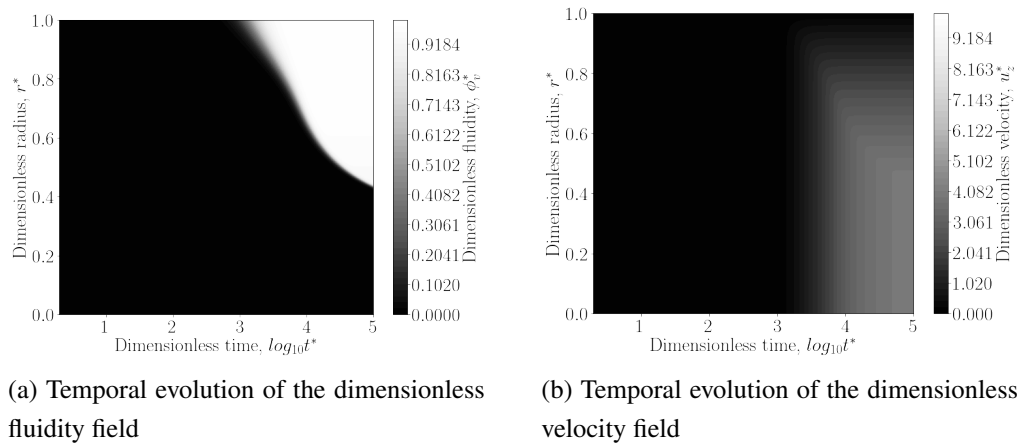
Figure 5.18: Simulation for $\frac{\Delta P}{L} = 9315.89$ Pa (0.4 Bar)

(a) Comparison between numerical and experimental results

(b) Numerical prediction for the mass flow rate

Figure 5.19: Comparison between numerical and experimental results for $\frac{\Delta P}{L} = 7974.3$ Pa (0.3 Bar)
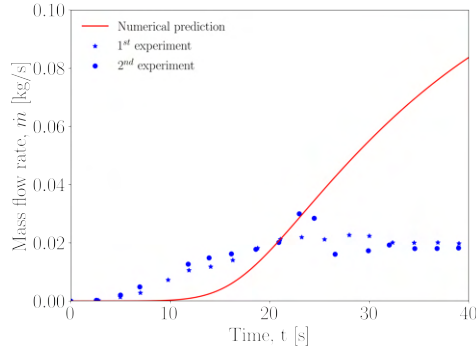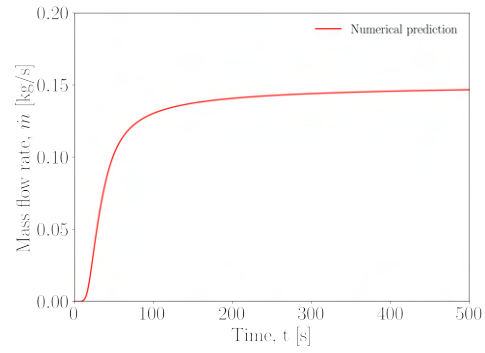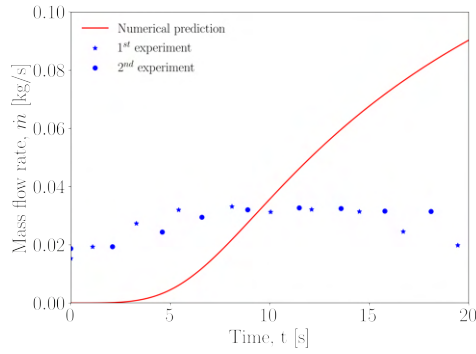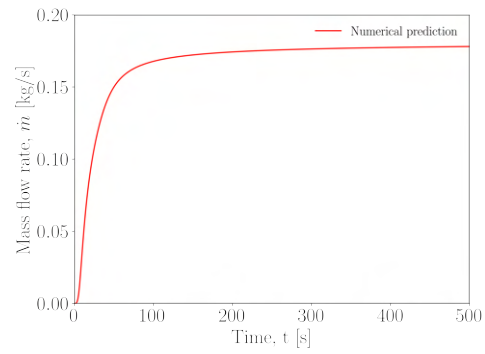

(a) Comparison between numerical and experimental results

(b) Numerical prediction for the mass flow rate

Figure 5.20: Comparison between numerical and experimental results for $\frac{\Delta P}{L} = 9315.89$ Pa (0.4 Bar)

6
Conclusions and future works

In this work, the flow restart of thixotropic fluids were examined both numerically and experimentally. First, a constitutive equation that accounted the thixotropic feature of a Laponite suspension 1.25% wt was obtained, according to the framework proposed by de Souza Mendes et Al. [2]. Subsequently, simulations of the flow restart process promoted by and imposed constant pressure difference were performed in order to evaluate the influence of the thixotropic feature in the flow of the fluid presented in sec. 2.1 and in the Laponite suspension 2% wt present in [2]. Lastly, an attempt was made to validate the mathematical model obtained in sec. 5.1 by performing restart flow experiments in the experimental apparatus presented in Fig. 2.7

The numerical analysis performed in sec. 5.2 highlighted that both fluids demonstrated different fluidity evolution patterns depending on thixotropy levels, with high thixotropy resulting in a gradual transition from rest to flow, while low thixotropy lead to abrupt transitions. Lower Pl values were associated with earlier flow restarts for both fluids and larger sheared regions along the spatial domain. Remarkably, Fluid B failed to reach steady-state within the simulation's time span, suggesting that other material properties may affect its rheological development. The comparison between the numerical predictions and experimental results showed considerable divergence; it is very likely that the great discrepancy found between the experimental data and the numerical predictions presented in sec. 5.3 are due to the physical limitations of the experimental apparatus. Nonetheless, the utilized mathematical model proved to be an essential and powerful tool for understanding the flow of thixotropic materials.

Currently, a new part for the experimental apparatus is being designed. It comprises a manufactured epoxi resin pipe obtained from a previously prepared silicon mold that was created to posses the form of half of a pipe with a grooved surface of 2.033 m length; this geometry was designed in a CAD software and printed in a stereolitography 3D printer. The pipe's groove is an entailed equilateral triangle with an edge length of 0.8 mm swept over the shape of an half pipe of 1 cm of diameter, as showed in Fig. 6.1. Then, the pipe is formed by assembling two of this half duct parts over each other. Also, six entries for attaching pressure transducers along this section have been included to obtain the pressure profile over the pipe length.

For future works, it is suggested to explore the following topics:

1. To use an experimental apparatus with the following alterations: a longer pipe
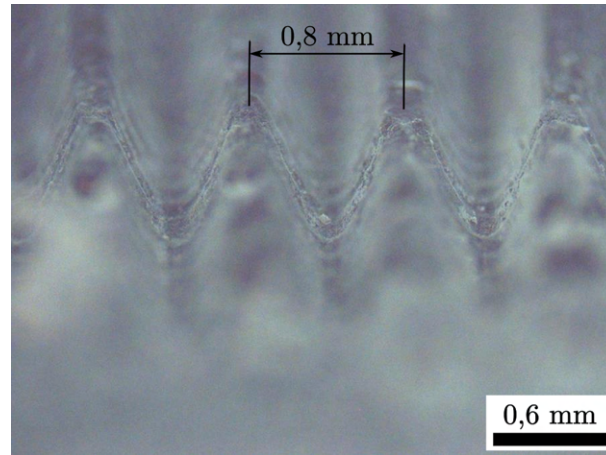
Figure 6.1: A picture of the epoxy resin pipe's grooved surface obtained using a Nikon Eclipse LV100N microscope.

section (4 m seems a reasonable length) and a larger tank with smooth walls, in order to let the piston push the fluid freely inside the pipeline;

2. To Simulate a 2D version of the physical situation mathematically modeled in Chapter 3, in order to analyze the influence of thixotropy in the pressure propagation;

3. To simulate the flow of TEVP fluids modeled with the constitutive equation proposed by de Souza Mendes et Al. [2] in complex flows, in order to analyze the influence of the interplay between viscoelasticity and thixotropy in physical variables of interest.

7
Bibliography

1   CUNHA J. P.; DE SOUZA MENDES, P. R.; SIQUEIRA, I. R. Pressure-driven flows of a thixotropic viscoplastic material: Performance of a novel fluidity-based constitutive model. ***Physics of Fluids***, v. 32, n. 12, 2020.

2   DE SOUZA MENDES, P. R.; ABEDI., B.; THOMPSON, R. L. Constructing a thixotropy model from rheological experiments. ***Journal of Non-Newtonian Fluid Mechanics***, v. 261, p. 1–8, 2018.

3   DE SOUZA MENDES P. R.; THOMPSON, R. L. Time-dependent yield stress materials. ***Current Opinion in Colloid & Interface Science***, v. 43, p. 15–25, 2019.

4   BIRD, R. B.; ARMSTRONG, R. C.; HASSAGER, O. **Dynamics of polymeric liquids. Vol. 1**: Fluid mechanics. John Wiley and Sons Inc., New York, NY, 1987.

5   BAIRD, D. G. **Encyclopedia of Physical Science and Technology**. Academic Press, New York, p. 611–643, 2003.

6   VINAY, G.; BHASKORO, P. T.; HENAUT, I; SARIMAN, M. Z.; ANUAR, A.; SHAFIAN, S. R. M. A methodology to investigate factors governing the restart pressure of a malaysian waxy crude oil pipeline. ***Journal of Petroleum Science and Engineering***, v. 208, 2022.

7   DOU, L.; WEN, Z.; WANG, J.; WANG, Z; HE, Z; LIU, X.; ZHANG, N. Analysis of the world oil and gas exploration situation in 2021. ***Petroleum Exploration and Development***, v. 49, n. 5, p. 1195–1209, 2022.

8   LUTHI, I. F. Waxy Crude Oil Characterization and Experimental Study of the Restart of a Line Blocked with Gelled Waxy Crude. ***SPE Annual Technical Conference and Exhibition***, 2013.

9   BOGER, D. V. Rheology of slurries and environmental impacts in the mining industry. ***Annual review of chemical and biomolecular engineering***, v. 4, p. 239–257, 2013.

10   SMOLDERS, A. J. P.; LOCK, R. A. C.; VAN DER VELDE, G.; MEDINA HOYOS, R. I.; ROELOFS, J. G. M. Effects of mining activities on heavy metal concentrations in water, sediment, and macroinvertebrates in different reaches of the pilcomayo river, south america. ***Archives of Environmental Contamination and Toxicology***, v. 44, p. 314–323, 2003.

11   DEMKOVÁ, L.; JEZNỲ, T.; BOBUĽSKÁ, L. Assessment of soil heavy metal pollution in a former mining area–before and after the end of mining activities. ***Soil and water Research***, v. 12, n. 4, p. 229–236, 2017.

12   MOURINHA, C; PALMA, P.; ALEXANDRE, C.; CRUZ, N.; RODRIGUES, S. M.; ALVARENGA, P. Potentially toxic elements' contamination of soils affected by

mining activities in the portuguese sector of the iberian pyrite belt and optional remediation actions: A review. ***Environments***, v. 9, n. 1, p. 11, 2022.

13   DO CARMO, F. F.; KAMINO, L. H. Y.; JUNIOR, R. T.; DE CAMPOS, I. C.; DO CARMO, F. F.; SILVINO, G.; MAURO, M. L.; RODRIGUES, N. U. A.; DE SOUZA MIRANDA, M. P.; PINTO, C. E. F. Fundão tailings dam failures: the environment tragedy of the largest technological disaster of brazilian mining in global context. ***Perspectives in ecology and conservation***, v. 15, n. 3, p. 145–151, 2017.

14   SOFRÀ, F.; BOGER, D. V. Environmental rheology for waste minimisation in the minerals industry. ***Chemical Engineering Journal***, v. 86, p. 319–330, 2002.

15   YILMAZ, E.; FALL, M. ***Paste tailings management***. [S.l.]: Springer, 2017.

16   DRECHSEL, P.; QADIR, M.; WICHELNS, D. ***Wastewater: economic asset in an urbanizing world***. [S.l.]: Springer, 2015.

17   The United Nations Environment Programme. ***For People and Planet: The United Nations Environment Programme strategy for tackling climate change, biodiversity and nature loss, and pollution and waste from 2022-2025***. [S.l.]: United Nations, 2020.

18   The United Nations Department of Economic and Social Affairs. ***World population prospects 2022: Summary of results***. [S.l.]: United Nations, 2023.

19   SEZGIN, M.; JENKINS, D.; PARKER, D. S. A unified theory of filamentous activated sludge bulking. ***Water Pollution Control Federation***, p. 362–381, 1978.

20   TIXIER, N.; GUIBAUD, G.; BAUDU, M. Towards a rheological parameter for activated sludge bulking characterisation. ***Enzyme and Microbial Technology***, Elsevier, v. 33, n. 2-3, p. 292–298, 2003.

21   DI CAPUA, F.; SPASIANO, D; GIORDANO, A.; ADANI, F.; FRATINO, U.; PIROZZI, F.; ESPOSITO, G. High-solid anaerobic digestion of sewage sludge: Challenges and opportunities. ***Applied Energy***, v. 278, 2020.

22   WORRELL, E.; PRICE, L.; MARTIN, N.; HENDRICKS, C.; MEIDA, L. O. Carbon dioxide emissions from the global cement industry. ***Annual review of energy and the environment***, v. 26, n. 1, p. 303–329, 2001.

23   AYTEKIN, B.; MARDANI-AGHABAGLOU, A. Sustainable materials: A review of recycled concrete aggregate utilization as pavement material. ***Transportation Research Record***, v. 2676, n. 3, p. 468–491, 2022.

24   ALDRED, J. Burj khalifa–a new high for high-performance concrete. ***Proceedings of the Institution of Civil Engineers-Civil Engineering***, v. 163, n. 2, p. 66–73, 2010.

25   GUILLOT, D. Rheology of well cement slurries. ***Developments in Petroleum Science***, Elsevier, v. 28, 1990.

26   ZHANG, Y.; ZHANG, Y.; LIU, G.; YANG, Y.; WU, M.; PANG, B. Fresh properties of a novel 3d printing concrete ink. ***Construction and building materials***, Elsevier, v. 174, p. 263–271, 2018.

27   ZHANG, Y.; ZHANG, Y.; SHE, W.; YANG, L.; LIU, G.; YANG, Y. Rheological and harden properties of the high-thixotropy 3d printing concrete. ***Construction and Building Materials***, Elsevier, v. 201, p. 278–285, 2019.

28   FERRARIS, C.; LARRARD, F. D.; MARTYS, N. Fresh concrete rheology: recent developments. ***Materials Science of Concrete VI, Amer. Cer. Soc. Ed. S. Mindess, J. Skalny***, p. 215–241, 2001.

29   DE SCHUTTER, G. Thixotropic effects during large-scale concrete pump test on site. ***International Conference on Advances in Construction Materials and Systems***, RILEM Publications, 2, p. 1–7, 2017.

30   CHALA, G. T.; SULAIMAN, S. A.; JAPPER-JAAFAR, A. Flow start-up and transportation of waxy crude oil in pipelines-a review. ***Journal of Non-Newtonian Fluid Mechanics***, v. 251, p. 69–87, 2018.

31   THOMASON, W. H. Start-Up and Shut-In Issues for Subsea Production of High Paraffinic Crudes. ***OTC Offshore Technology Conference***, 2000.

32   SENTJABRSKAJA, T.; CHAUDHURI, P.; HERMES, M.; POON, W. C. K.; HORBACH, J. EGELHAAF, S. U.; LAURATI, M. Creep and flow of glasses: Strain response linked to the spatial distribution of dynamical heterogeneities. ***Scientific reports***, Nature Publishing Group UK London, v. 5, n. 1, p. 11884, 2015.

33   CIPELLETTI, L.; MARTENS, K.; RAMOS, L. Microscopic precursors of failure in soft matter. ***Soft matter***, Royal Society of Chemistry, v. 16, n. 1, p. 82–93, 2020.

34   LANDRUM, B. J.; RUSSEL, W. B.; ZIA, R. N. Delayed yield in colloidal gels: Creep, flow, and re-entrant solid regimes. ***Journal of Rheology***, The Society of Rheology, v. 60, n. 4, p. 783–807, 2016.

35   GRENARD, V.; DIVOUX, T.; TABERLET, N.; MANNEVILLE, S. Timescales in creep and yielding of attractive gels. ***Soft matter***, Royal Society of Chemistry, v. 10, n. 10, p. 1555–1571, 2014.

36   CATON F.; BARAVIAN, C. Plastic behavior of some yield stress fluids: from creep to long-time yield. ***Rheologica Acta***, Springer, v. 47, n. 5-6, p. 601–607, 2008.

37   VISINTIN, R. F. G.; LAPASIN, R.; VIGNATI, E.; D'ANTONA, P.; LOCKHART, T. P. Rheological behavior and structural interpretation of waxy crude oil gels. ***Langmuir***, ACS Publications, v. 21, n. 14, p. 6240–6249, 2005.

38   LIU, W.; ZHU, K. A study of start-up flow of thixotropic fluids including inertia effects on an inclined plane. ***Physics of Fluids***, AIP Publishing, v. 23, n. 1, 2011.

39   QIAN Y.; KAWASHIMA, S. Distinguishing dynamic and static yield stress of fresh cement mortars through thixotropy. *Cement and Concrete Composites*, Elsevier, v. 86, p. 288–296, 2018.

40   CHANG C.; BOGER, D. V. N. Q. D. The yielding of waxy crude oils. *Industrial & engineering chemistry research*, ACS Publications, v. 37, n. 4, p. 1551–1559, 1998.

41   FAKROUN A.; BENKREI, H. Rheology of waxy crude oils in relation to restart of gelled pipelines. *Chemical Engineering Science*, Elsevier, v. 211, p. 115212, 2020.

42   THOMPSON, R. L.; SOARES, E. J. Viscoplastic dimensionless numbers. *Journal of Non-Newtonian Fluid Mechanics*, Elsevier, v. 238, p. 57–64, 2016.

43   WANG, Y.; MAGDA, J.; VENKATESAN, R.; SAMBATH, K.; DEO, M. Experimental and theoretical investigations of waxy crude oil in steady and transient pipe flows. *Industrial & Engineering Chemistry Research*, ACS Publications, v. 59, n. 30, p. 13783–13798, 2020.

44   MOISÉS, G.V.L.; ALENCAR, L.S.; NACCACHE, M.F.; FRIGAARD, I.A. The influence of thixotropy in start-up flow of yield stress fluids in a pipe. *Journal of Petroleum Science and Engineering*, v. 171, p. 794–807, 2018.

45   ABEDI, B.; MENDES, R.; DE SOUZA MENDES, P. R. Startup flow of yield-stress non-thixotropic and thixotropic materials in a tube. *Journal of Petroleum Science and Engineering*, v. 174, p. 437–445, 2019.

46   SCHALEK, F. E.; SZEGVARY, A. Ueber eisenoxydgallerten: Vorläufige mitteilung. *Kolloid-Zeitschrift*, Springer, v. 32, p. 318–319, 1923.

47   LARSON R. G.; WEI, Y. A review of thixotropy and its rheological modeling. *Journal of Rheology*, The Society of Rheology, v. 63, n. 3, p. 477–501, 2019.

48   MEWIS, J.; WAGNER, N. J. Thixotropy. *Advances in colloid and interface science*, Elsevier, v. 147, p. 214–227, 2009.

49   BARNES, H. A. Thixotropy—a review. *Journal of Non-Newtonian fluid mechanics*, Elsevier, v. 70, n. 1-2, p. 1–33, 1997.

50   LIVESCU, S. Mathematical modeling of thixotropic drilling mud and crude oil flow in wells and pipelines—a review. *Journal of Petroleum Science and Engineering*, v. 98-99, p. 174–184, 2012.

51   FRIGAARD, I. A.; PASO, K. G.; MENDES, P. R. de S. Bingham's model in the oil and gas industry. *Rheologica Acta*, v. 56, p. 259–282, 2017.

52   GOODEVE, C.; WHITFIELD, G. The measurement of thixotropy in absolute units. *Transactions of the Faraday Society*, Royal Society of Chemistry, v. 34, p. 511–520, 1938.

53   GOODEVE, C. F. A general theory of thixotropy and viscosity. *Transactions of the Faraday Society*, Royal Society of Chemistry, v. 35, p. 342–358, 1939.

54   ACIERNO, D; LA MANTIA, F. P.; MARRUCCI, G.; TITOMANLIO, G. A non-linear viscoelastic model with structure-dependent relaxation times: I. basic formulation. ***Journal of Non-Newtonian Fluid Mechanics***, Elsevier, v. 1, n. 2, p. 125–146, 1976.

55   MUJUMDAR, A.; BERIS, A. N.; METZNER, A. B. Transient phenomena in thixotropic systems. ***Journal of Non-Newtonian Fluid Mechanics***, Elsevier, v. 102, n. 2, p. 157–178, 2002.

56   DE SOUZA MENDES, P. R. Modeling the thixotropic behavior of structured fluids. ***Journal of Non-Newtonian Fluid Mechanics***, v. 164, n. 1, p. 66–75, 2009.

57   DE SOUZA MENDES, P. R.; THOMPSON, R. L. A critical overview of elasto-viscoplastic thixotropic modeling. ***Journal of Non-Newtonian Fluid Mechanics***, v. 187-188, p. 8–15, 2012.

58   THOMPSON, R. L. The eagle and the rat: Non–equilibrium dynamics in time-dependent materials. ***Journal of Non-Newtonian Fluid Mechanics***, Elsevier, v. 281, p. 104313, 2020.

59   DE SOUZA MENDES, P. R. Thixotropic elasto-viscoplastic model for structured fluids. ***Soft Matter***, v. 7, p. 2471–2483, 03 2011.

60   DE SOUZA MENDES, P. R.; THOMPSON, R. L. A unified approach to model elasto-viscoplastic thixotropic yield-stress materials and apparent yield-stress fluids. ***Rheologica Acta***, Springer, v. 52, p. 673–694, 2013.

61   ABEDI, B. ***Startup Flow of Gelled Crude Oils: an Experimental Study****. Advisor: Paulo Roberto de Souza Mendes. Rio de Janeiro, 2016. 62 p.* Dissertação (Mestrado) — Graduate Program in Mechanical Engineering, Pontifical Catholic University of Rio de Janeiro, Rio de Janeiro, Brazil, 2016.

62   DE SOUZA MENDES, P. R. Dimensionless non-newtonian fluid mechanics. ***Journal of non-Newtonian fluid mechanics***, Elsevier, v. 147, n. 1-2, p. 109–116, 2007.

63   CELIK, I. B.; GHIA, U.; ROACHE, P. J.; FREITAS, C.J.; COLEMAN, H.; RAAD, P.E. Journal of fluids engineering editorial policy statement on the control of numerical accuracy. 2000.

64   VERSTEEG, H. K.; MALALASEKERA, W. ***An introduction to computational fluid dynamics: the finite volume method***. [S.l.]: Pearson education, 2007.